Article

Modular chiral origami metamaterials

Tuo Zhao[1,5], Xiangxin Dang[1,5], Konstantinos Manos[2], Shixi Zang[1], Jyotirmoy Mandal[1,3], Minjie Chen[2,4] & Glaucio H. Paulino[1,3 ✉]

Metamaterials with multimodal deformation mechanisms resemble machines[1,2], especially when endowed with autonomous functionality. A representative architected assembly, with tunable chirality, converts linear motion into rotation[3]. These chiral metamaterials with a machine-like dual modality have potential use in areas such as wave manipulation[4], optical activity related to circular polarization[5] and chiral active fluids[6]. However, the dual motions are essentially coupled and cannot be independently controlled. Moreover, they are restricted to small deformation, that is, strain ≤2%, which limits their applications. Here we establish modular chiral metamaterials, consisting of auxetic planar tessellations and origami-inspired columnar arrays, with decoupled actuation. Under single-degree-of-freedom actuation, the assembly twists between 0° and 90°, contracts in-plane up to 25% and shrinks out-of-plane more than 50%. Using experiments and simulations, we show that the deformation of the assembly involves in-plane twist and contraction dominated by the rotating-square tessellations and out-of-plane shrinkage dominated by the tubular Kresling origami arrays. Moreover, we demonstrate two distinct actuation conditions: twist with free translation and linear displacement with free rotation. Our metamaterial is built on a highly modular assembly, which enables reprogrammable instability, local chirality control, tunable loading capacity and scalability. Our concept provides routes towards multimodal, multistable and reprogrammable machines, with applications in robotic transformers, thermoregulation, mechanical memories in hysteresis loops, non-commutative state transition and plug-and-play functional assemblies for energy absorption and information encryption.

Mechanical metamaterials are architected macroscopic structures assembled with desired geometrical arrangements leading to unusual mechanical properties and deformation modes. The macroscopic properties of metamaterials depend on the specific shape, size and geometric orientation of the mesoscale unit cells[7]. Classic architected cells, such as the stretching-dominated octet-truss unit[8,9] and the bending-dominated Kelvin lattice[10,11], have been explored in applications[12], including ultralight systems[13], extreme energy dissipation[14] and lattice fracture characterization[15]. Chirality, a concept established in several fields[16], has also been used to create material systems. Metamaterials composed of chiral unit cells have enabled unusual deformation effects[17], such as the coupling between strain and twist[3,18]. The aforementioned mechanical metamaterials assume perfectly rigid connections between all unit cells; thus, the deformation kinematics remains in the geometrically linear region. By contrast, reconfigurable assemblies, for example, origami- and kirigami-inspired metamaterials[19–22], expand the motion into finite deformation for applications involving shape morphing[23,24]. Three-dimensional reconfigurability is achieved by connecting unit cells with flexible hinges arranged in both in-plane and out-of-plane directions[25–27]. However, the geometrical nonlinearity of flexible connections introduces multiple degrees of freedom into the metamaterial, which relies on an integrated system or external stimuli for actuation[28–31]. Moreover, most reconfigurable metamaterials focus on effective physical properties under uniaxial deformation[32]. Multimodal assemblies with an easy-to-actuate single-degree-of-freedom mechanism could lead to synergism between material and robotic functionalities, as explored in this work.

Here we introduce a reconfigurable metamaterial, accommodating origami-inspired chiral arrays and mechanism-inspired auxetic tessellations, that reconciles translation and rotation for distinct actuation modes, that is, twist with free translation or linear displacement with free rotation. In either mode, our reconfigurable assembly can contract or reversely expand in three orthogonal directions on demand by single-degree-of-freedom actuation, accomplished by special fixtures. The contraction or expansion is accompanied by the twist of the tessellation, the direction of which is dictated by the chirality of the arrays.

Our metamaterial is achieved using a modular assembling scheme, endowed with high modularity and reprogrammability. Modular metamaterials are generally assembled from discrete components at the local level that can produce desired elastic behaviours, including near-zero or negative Poisson's ratio[33], continuously variable modulus[34] and tunable instability[35,36]. In our case, the loading capacities and energy envelopes of the metamaterial can be systematically reprogrammed by selecting the proper geometry, chirality and materials of the modular

[1]Department of Civil and Environmental Engineering, Princeton University, Princeton, NJ, USA. [2]Department of Electrical and Computer Engineering, Princeton University, Princeton, NJ, USA. [3]Princeton Materials Institute, Princeton University, Princeton, NJ, USA. [4]Andlinger Center for Energy and the Environment, Princeton University, Princeton, NJ, USA. [5]These authors contributed equally: Tuo Zhao, Xiangxin Dang. ✉e-mail: gpaulino@princeton.edu
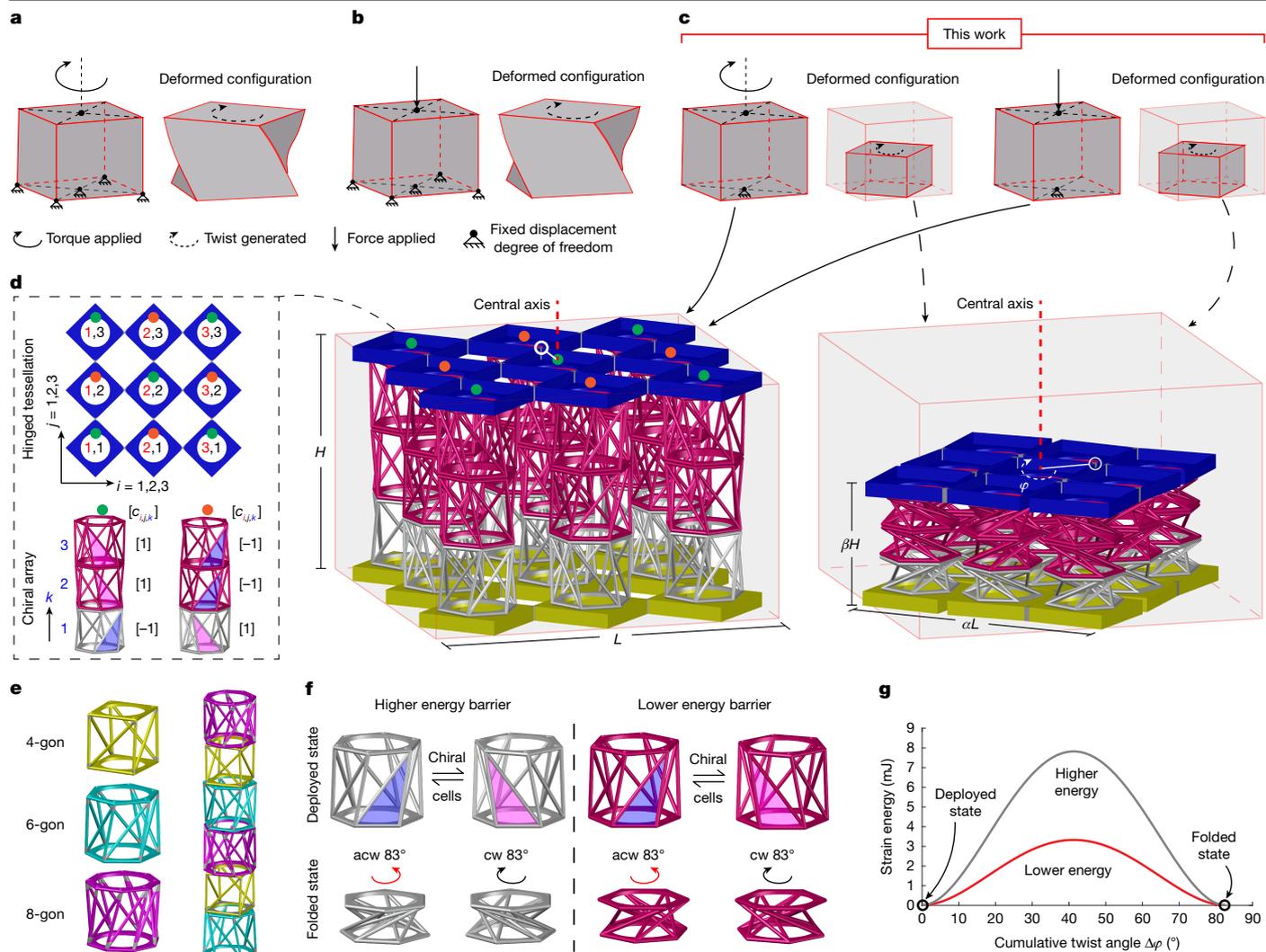
Fig. 1 | The multimodal metamaterial composed of hinged tessellations and chiral origami-inspired lattice cells. a, Twisting deformation of standard elastic material on application of torque. **b**, A representative twisting metamaterial under compression[3]. **c**, Multimodal deformation mechanism actuated by two independent testing conditions, that is, twist with free translation and linear displacement with free rotation. **d**, Schematic of the metamaterial assemblies in the undeformed configuration (left) and the deformed configuration (right), respectively. The assembly consists of hinged tessellations (blue and yellow) and arrays of origami-inspired unit cells (red and grey). L, edge length; H, height; $\varphi \in [0°, 90°]$, twist angle; $\alpha \in [0, 1]$, length change scalar; and $\beta \in (0, 1]$, height change scalar. The inset shows the chirality assignment of modular cells in the assembly. **e**, A family of rod-based lattice cells with kinematically compatible geometries, for example, 4-gon, 6-gon and 8-gon cells. **f**, Two sets of chiral unit cells with distinguishable energy barriers. acw, anticlockwise twist; cw, clockwise twist. **g**, The stored strain energy versus the change of twist angle for unit cells. The red curve and the grey curve represent the energy envelope for the lower-energy-barrier cell and the higher-energy-barrier cell, respectively. The energy calculation is based on the parameters (red and white cells) defined in Methods, 'Simulation'.

cells. We can achieve target mechanical response, for example, the number of stable states and distinct energy barriers, using desired actuation modes.

The multimodal, multistable and reprogrammable features of our proposed modular chiral metamaterial enable a diverse range of applications. In the domain of mechanics, we demonstrate mechanical hysteresis loops and non-commutative state transitions, both of which are rooted in the history-dependent deformations of the modular metamaterial. We also build plug-and-play functional assemblies for energy absorption and information encryption. Beyond mechanics, we integrate magnetic, thermal and optical materials into our multimodal assemblies, exploring interdisciplinary applications, including dual-mode robots combining locomotion and transformation and thermoregulation of buildings for energy consumption reduction.

Multimodal deformation with decoupled actuation

Standard elastic materials have a single deformation mode, for example, they generate twists when torque is applied (Fig. 1a). For comparison, architected materials reveal new kinematics with multimodal deformation mechanisms. When compressed, the metamaterial[3] converts linear motion into rotation (Fig. 1b). This rotational deformation is coupled with the translational deformation, and the corresponding compressive strain is within the linear elastic regime. To enhance the multimodal motion ability of metamaterials for large deformations, we build an auxetic assembly of which the cross-section can twist between 0° and 90°, accompanied by a contraction of up to 25%, whereas the height shrinks more than 50%. Unlike other metamaterials responding to a single loading condition, our architected assembly deforms under two independent actuation conditions: twist with free translation

and linear displacement with free rotation (Fig. 1c). This unique multimodal deformation mechanism is enabled by an arrangement that involves origami-inspired chiral columnar arrays assembled with mechanism-inspired tessellations on top and bottom (Fig. 1d). The columnar array is modular and composed of panel-free deformable chiral cells (Supplementary Information section 1 and Supplementary Fig. 1). Each square in the tessellation rotates relative to its adjacent squares by the same twist angle (Supplementary Fig. 2). Confined by the tessellation, all the columns should have the same height and twist angle throughout the deformation (Supplementary Information section 2). The chirality assignment in neighbouring columns is reversed to fit the opposite rotation direction of the panels (that is, −1, 1, 1 in the column indicated by the green dots compared with 1, −1, −1 in the column indicated by the red dots in Fig. 1d). Here, +1 and −1 represent the chirality consistent with the clockwise twisting and the anticlockwise twisting, respectively. Because of the supermodular nature of the assembly, the specific chirality assignment can be generalized for a scaled-up system, including tessellations of I-by-J (rotating) squares and columns of K cells, by the following formula:

$$c_{i,j,k} = c_k r_{i,j} \text{ in which } c_k = (-1)^{\left\lceil \frac{k+1}{2} \right\rceil} \text{ and } r_{i,j} = (-1)^{[(i+j)\bmod 2]}, \quad (1)$$

where the operation $\lceil (k+1)/2 \rceil$ gives the smallest integer greater than or equal to $(k+1)/2$, the operation $(i+j) \bmod 2$ gives the remainder of Euclidean division of $i+j$ by 2, the indices range in $i = 1, …, I, j = 1, …, J$ and $k = 1, …, K$. The bivalued number $c_{i,j,k}$ indicates the chirality of the kth cell in the column attached to the panel i, j. The proper geometry (Fig. 1e), chirality assignments (Fig. 1f) and material selection (Fig. 1g) contribute to desired modular cell properties (Methods, 'Basic modules and properties', and Extended Data Fig. 1). Supplementary Fig. 3 demonstrates the chirality assignments for assemblies with increasing system sizes, that is, $I, J, K \geq 4$ (Supplementary Information section 3).

Experimental setups and results

In one instance, we show that the metamaterial twists, contracts or expands and shrinks using rotational actuation with free translation (Extended Data Fig. 2b). The twist experiment has three loading steps (Fig. 2a). In step one, the actuator rotates by −83° (acw), generating twisting deformation of the metamaterial. Naturally, the edge contracts and the height shrinks. In step two, the actuator rotates by 83° (cw), the height continues shrinking, and the edge expands. In step three, the actuator rotates by 83° (cw), and the edge length and the height eventually reduce. Finally, the net twist is 83° (cw), whereas the cumulative twist is 249°. Figure 2b illustrates four representative configurations of the experiment (Supplementary Video 1). It is worth noting that the global twisting deformation is controlled by the rotational actuator, whereas the twist of the modular units depends on the chiral arrangement (Fig. 2c). The torque sensor measures the responses of the assembly to the pre-programmed rotational loading sequences (Fig. 2d). From the kinematics perspective, we compare the theoretical deformation with the testing data measured from the snapshots of the recording of the experiment (Fig. 2e and Methods, 'Experiments'). We find that the theory predicts well the in-plane deformation, for example, edge contraction or expansion, as well as the out-of-plane deformation, for example, height shrinkage (Supplementary Information section 2). We observe that our modular metamaterial allows the variation of the number of layers (see Supplementary Fig. 4 for single- and double-layer experiments) and the number of chiral cells per layer.

In another instance, we explore the behaviour of the chiral metamaterial by using a linear displacement actuation with free rotation. The behaviour of the entire assembly depends heavily on the boundary conditions of the experimental setup (see Fig. 3, Supplementary Information section 4 and Supplementary Figs. 5 and 6). The selected

boundary conditions of Fig. 3a show a top free-rotating plate and a bottom fixed plate that are connected to the rotating squares using micro-rollers with ball transfer. The configurations of Fig. 3b demonstrate the multimodal deformations of the assembly as shown in Supplementary Video 2. From state (1) to (2), the assembly shrinks in the axial direction and barely twists. From state (2) to (3), the assembly keeps shrinking and intensely rotates more than 60°. This is shown by the force–displacement profile of Fig. 3c (with the representative states of Fig. 3b) and the in-plane (edge contraction) and the out-of-plane (height shrinkage) deformation of Fig. 3d. For comparison, Supplementary Fig. 7 shows a functionally graded metamaterial tested under the same actuation and boundary conditions.

Modelling and simulation

Inspired by the bar and hinge model[37,38], we propose a surrogate model to simulate and provide insight into the multimodal deformations of the metamaterials (Methods, 'Simulation'). The simulation can be done for the unit cells (Extended Data Fig. 3), the modular columns (Extended Data Fig. 4) and the assemblies with rotating-square tessellations (Fig. 4).

We investigate three-layer columns and show that their final states are affected by the material and the chirality assignments. In Extended Data Fig. 4a, we provide the curves of torque versus cumulative twist angle of the three-layer modular columns under twisting. The anticlockwise twisting is compatible with the chirality of the bottom cell, which, therefore, always collapses first, regardless of its (larger) stiffness (Extended Data Fig. 4a,b). After the double clockwise twisting, the one-white-two-red column completely collapses, whereas the two-white-one-red column does not, leaving only one folded red cell. This discrepancy is caused by the free-translation boundary condition, which allows the columns to seek minimum energy in the height direction. This phenomenon is validated by the twisting experiment shown in Extended Data Fig. 5.

In Extended Data Fig. 4c, we provide the force–displacement curves of the three-layer modular columns under compression. The column with all red cells shows three peak forces of similar amplitudes, whereas the column with cells of all three different colours shows three peak forces of different amplitudes. The other two columns with only white and red cells (one-white-two-red and two-white-one-red) show two similar peaks and the third peak of different heights. All the columns are compressed to the collapsed states (Extended Data Fig. 4d). Although here we study the columns with the same chirality assignment and different materials, we refer to Supplementary Video 3 for the opposite situation, that is, columns with different chirality assignments and the same materials under either compression or twisting.

The deformation simulation of the assembly under twisting or compression loading is consistent with the experimental results. For the assembly under twist with free translation (Fig. 4a,b), we obtain the curves of torque versus cumulative twist angle (Fig. 4c), strain energy versus cumulative twist angle (Fig. 4d), and the volume change ratio versus cumulative twist angle (Fig. 4e). The deformation snapshots (Fig. 4b) and the trend of the torque variation (Fig. 4c, inset) qualitatively agree with the experimental results in Fig. 2b,d, respectively, featuring sequential folding of the white and red cells and three local peaks on the torque curves.

For the assembly under compression with free rotation (Fig. 4f,g), we obtain the curves of force versus displacement (Fig. 4h), strain energy versus displacement (Fig. 4i) and the volume change ratio versus displacement (Fig. 4j). The twist angle sweeps around 63° in the simulation (Fig. 4h, inset), which matches the experiment (Fig. 3b). The deformation snapshots (Fig. 4g) and the trend of the force variation (Fig. 4h) qualitatively relate to the experimental results in Fig. 3b,c, respectively, featuring simultaneous folding of red and white cells and two local peaks of the force curves. The simultaneous folding is induced from the constraint of the plates. For either the twisting or the compression
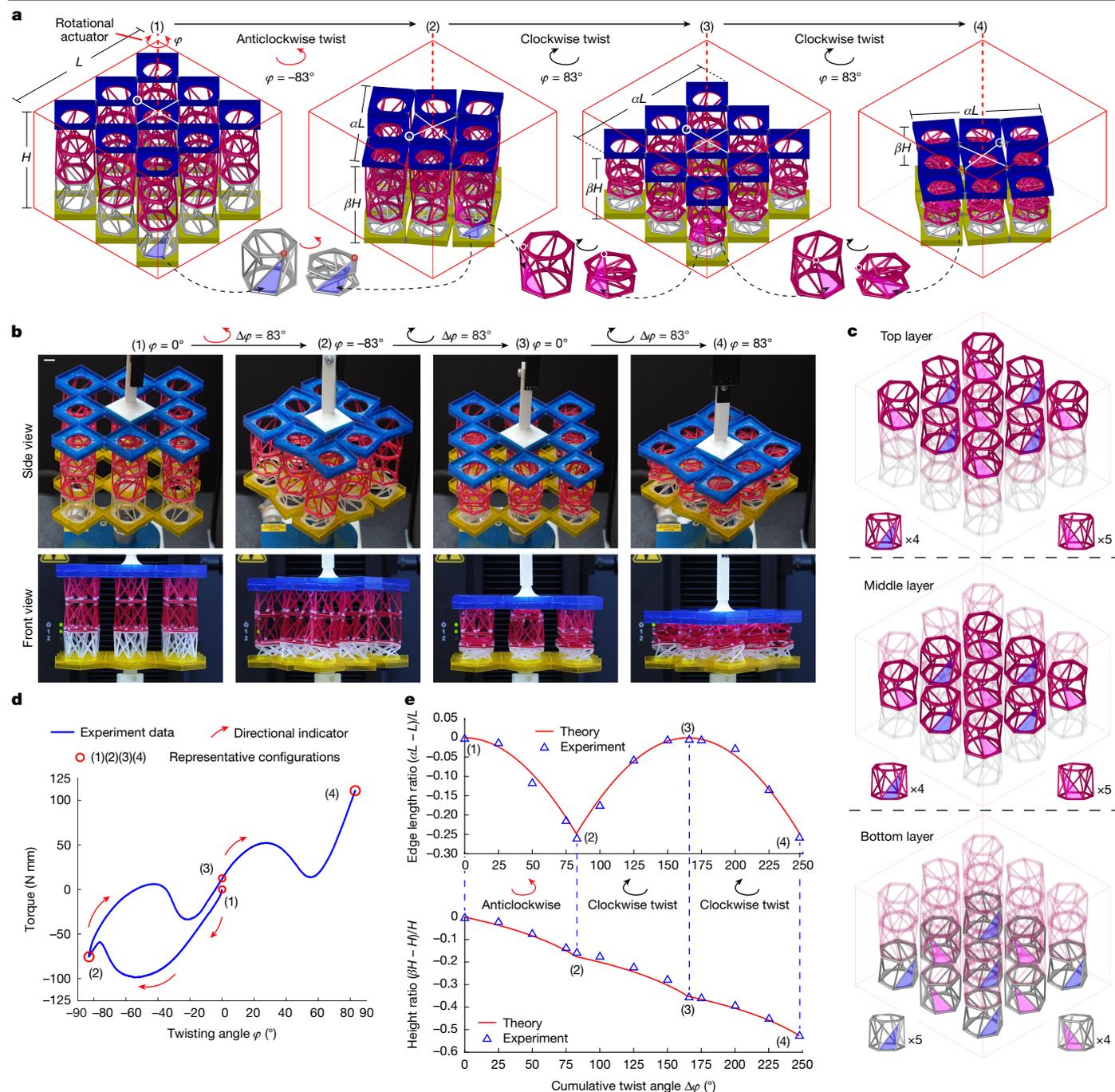
Fig. 2 | Experimental validation of multimodal deformation using a rotational actuator with free translation. a, Schematics of the four representative configurations following the rotational loading sequence, that is, anticlockwise twist −83°, then clockwise twist 83° and finally clockwise twist 83°. **b**, Mechanical testing of the triple-layer assembly. Insets are the representative configurations filmed from the side views (top row) and the front view (bottom row), respectively. Scale bar, 10 mm. **c**, Layer composition of the metamaterial in the initial undeformed configuration. **d**, Measured curve of torque versus twist angle with labels of the four representative states. The red arrows indicate the rotation sequence applied during the test. **e**, Assembly edge length change versus cumulative twist angle (top) and assembly height change versus cumulative twist angle (bottom), comparing representative testing data points with theoretical kinematics analyses (Supplementary Information section 2).

simulation, the strain energy of the final configuration reasonably matches the experimental results (Fig. 4d,i). The simulated deformation animations are provided in Supplementary Video 3.

Reprogrammable modular assemblies

Guided by our understanding of origami-inspired array simulation (Extended Data Fig. 4c,d) and experiments (Supplementary Figs. 9 and 10), we harness its highly nonlinear behaviour to design metamaterials with desired mechanical properties. The lattice cells can be connected to arrays, which can be further constructed into three-dimensional assemblies following a plug-and-play building strategy (Fig. 5a). The modular dipole is composed of two cells with opposite chirality, which displays twisting deformation at the middle layer of the dipole geometry (Fig. 5b). We select three materials with different elastic moduli to fabricate the dipoles, which have distinguishable loading
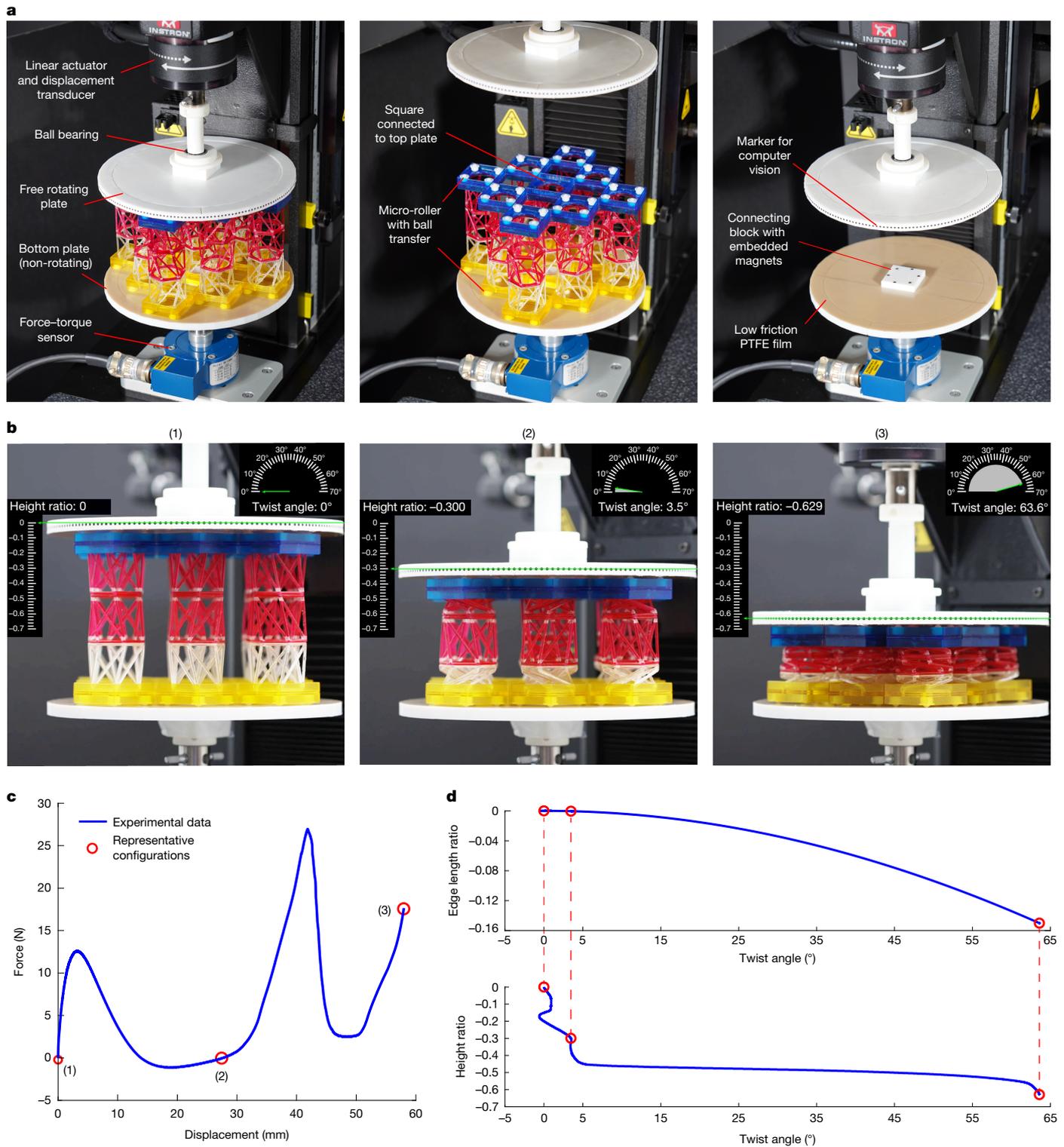
Fig. 3 | Experiment of multimodal deformation using a linear displacement actuation with free rotation. a, Detailed testing setup showing boundary conditions and loading. **b**, Three representative configurations. In each image, the vertical scale bar indicates the height change ratio of the assembly, and the arc scale bar shows the twist angle of the assembly. **c**, Measured force–displacement curve with labels of the representative states. **d**, Assembly edge length change versus twist angle (top) and assembly height change versus twist angle (bottom).

capacities and energy barriers (Fig. 5c). Given the 21 dipoles, we design the first assembling rule as shown in Fig. 5d for the metamaterial in Fig. 5e. The compression experiment shows that the three-dimensional (3D) assembly has four stable states highlighted in the displacement–force curve in Fig. 5f (left). Moreover, the peak load for each stable

configuration increases gradually. The corresponding accumulated strain energy is shown in Fig. 5f (right). These mechanical properties of the assembly can be reprogrammed by selecting an alternative assembling rule, for example, as shown in Fig. 5g. The new assembly (Fig. 5h) is made up of the same amount of dipoles as the assembly in Fig. 5e.
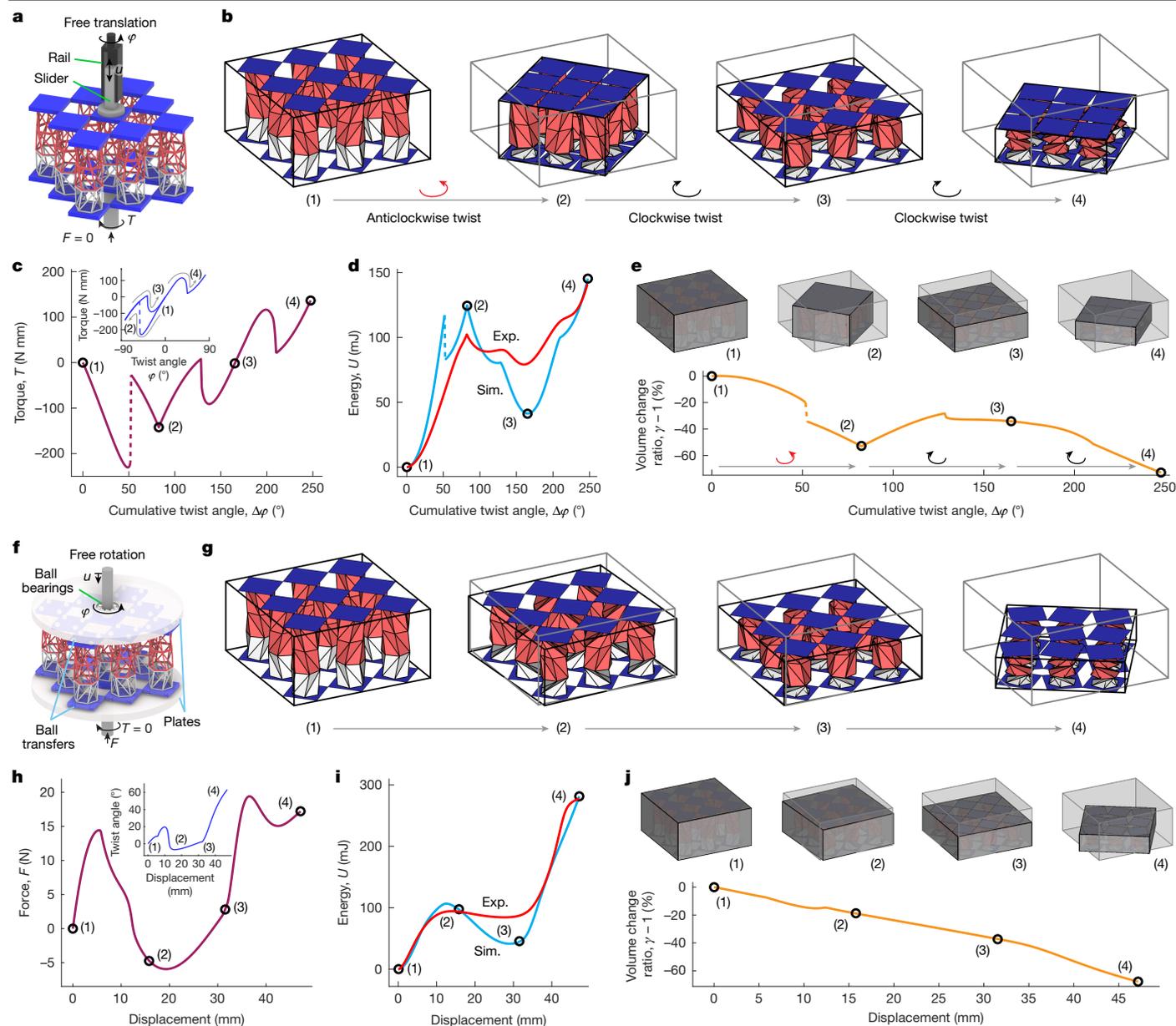
Fig. 4 | Surrogate model simulation for multimodal deformations of the modular assembly. a, Twisting simulation setup. **b**, Deformation snapshots (1)–(4) of the assembly. **c**, Curve of torque versus cumulative twist angle. The inset is the curve of torque versus twist angle that is defined as negative for anticlockwise rotation and positive for clockwise rotation. **d**, Curve of energy versus cumulative twist angle. **e**, Curve of volume change ratio versus cumulative twist angle and the enclosed volume of the snapshots (1)–(4). The dashed lines represent the sudden change of configuration induced from mechanical instability. **f**, Compression simulation setup. **g**, Deformation snapshots (1)–(4) of the assembly. **h**, Curve of force versus displacement. The inset is the curve of twist angle versus displacement. **i**, Curve of energy versus displacement. **j**, Curve of volume change ratio versus displacement and the enclosed volume of the snapshots (1)–(4).

However, the mechanical behaviour is quite different. In this case, the peak load of the new assembly in each stable state is almost identical. Furthermore, we find that the loading capacity at any stable state can be reprogrammed as shown in Fig. 5j–o and Supplementary Fig. 11. These features are shown in Supplementary Video 4.

Untethered robotic metamaterials

The inclusion of magnetic dipole elements within the multimodal assembly enables its remote actuation and manipulation in the presence of a controlled magnetic field. By leveraging the interaction between the external field and the dipole elements, an untethered robotic metamaterial emerges, capable of both locomotion and transformation between various states, that is, locomotion mode, transformer mode and transformer–locomotion mode (see Supplementary Video 5).

Inspired by advances in robotic metamaterials[39–42], we create a four-column and two-layer assembly, as shown in Fig. 6a. Cylindrical NdFeB permanent magnets with an out-of-plane magnetization are installed both on the individual chiral cells and on the top and bottom square tessellations serving two roles. First, they ensure the structural integrity of the assembly by holding the individual units together. Second, they contribute a total out-of-plane magnetization enabling the precise locomotion of the structure in any direction (Fig. 6a, left). This is achieved by imposing a rotating magnetic field generated by a three-dimensional Helmholtz-coil system (Extended Data Fig. 6 and Supplementary Information section 6). Next, we turn
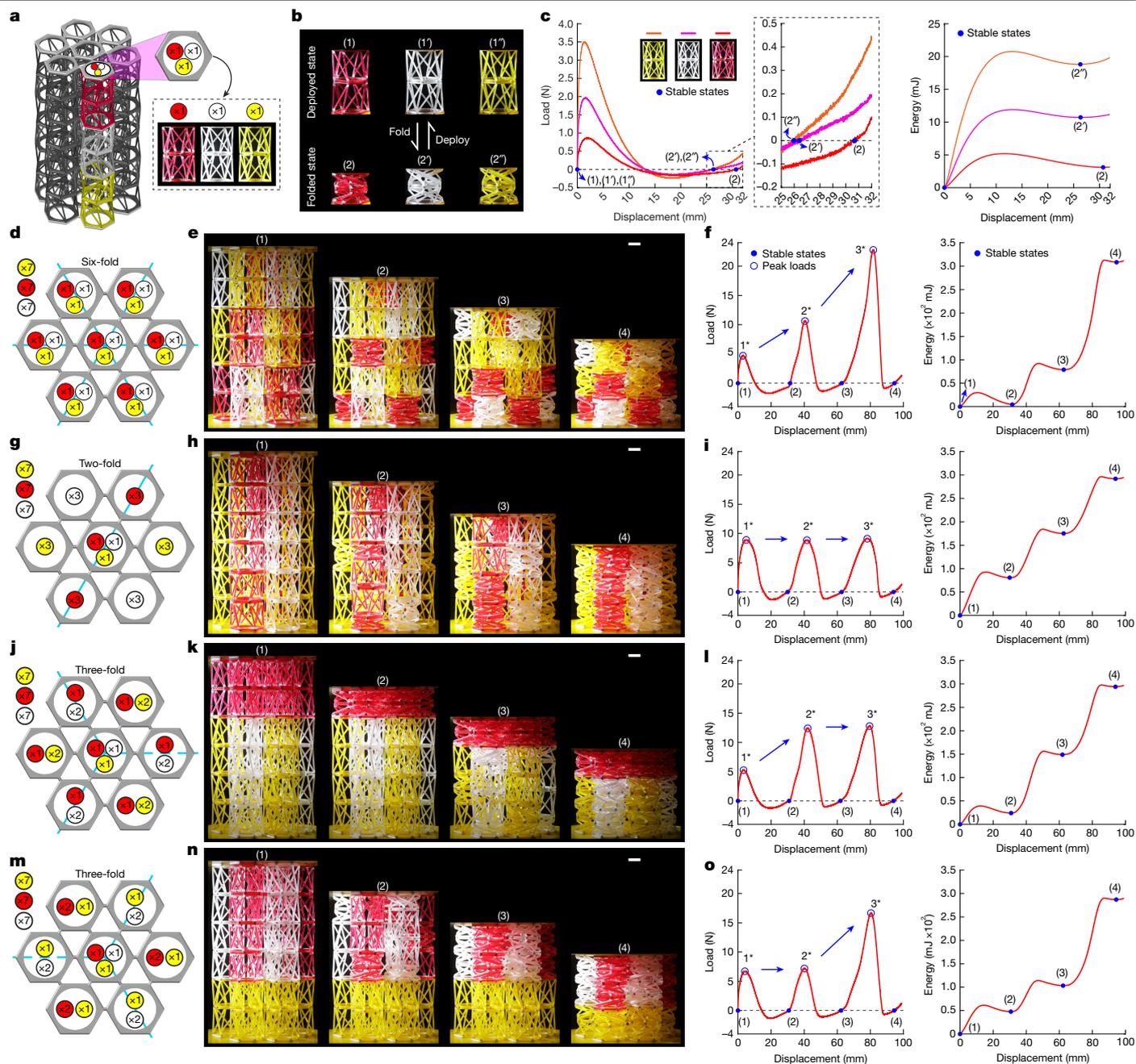
Fig. 5 | Plug-and-play strategy for creating reprogrammable metamaterials.
a, Schematic of the architected assembly consisting of three types of modular dipoles fabricated using red, white and yellow resins. **b**, Three 3D-printed dipoles in deployed and folded states, respectively. The diameter of the rods is 1.5 mm. **c**, Left, measured load–displacement curves for the three dipoles. The positions of the stable states are labelled using the blue dots on the curves. Right, stored energy of the dipoles versus displacement. The energy is determined by calculating the area under the load–displacement graphs. **d**, Top view of a six-fold assembly composed of 21 modular dipoles (7 each in yellow, red and white). The schematic provides instructions for assembling the dipoles. **e**, Four stable states of the assembly in **d**. **f**, Mechanical properties of the assembly in **d**. Left, measured load–displacement curve with labels of the four representative states in **e**. The peak loads of stable states (1), (2) and (3) are labelled as 1*, 2* and 3*, respectively. Right, stored energy of the assembly versus vertical displacement. **d–o**, Various assembly configurations made of the same group of modular units, corresponding stable states, measured load–displacement curves and corresponding energy landscapes. Scale bar, 10 mm (**e,h,k,n**).

to the transformer mode. By installing additional square magnetic plates with an in-plane magnetization on the tessellations (top and bottom), it is possible to trigger the transformer mode of the structure and selectively fold and deploy each of the layers, as shown in Fig. 6a (centre). This is accomplished by generating a one-dimensional field along the x-axis that induces out-of-plane torques on each plate, resulting in the twisting of the metamaterial. Finally, we turn to the combined transformer–locomotion mode. The locomotion of the

metamaterial in the compressed state is realized by generating a rotating 3D magnetic field Fig. 6a (right). This mode is enabled by leveraging the net magnetization of the assembly arising from the contribution of both the magnetic plates and the cylindrical permanent magnets.

Together, these three modes of actuation highlight the versatility of the proposed robotic metamaterial. When encountering confined spaces, the assembly can fold (contract) and move to its destination.
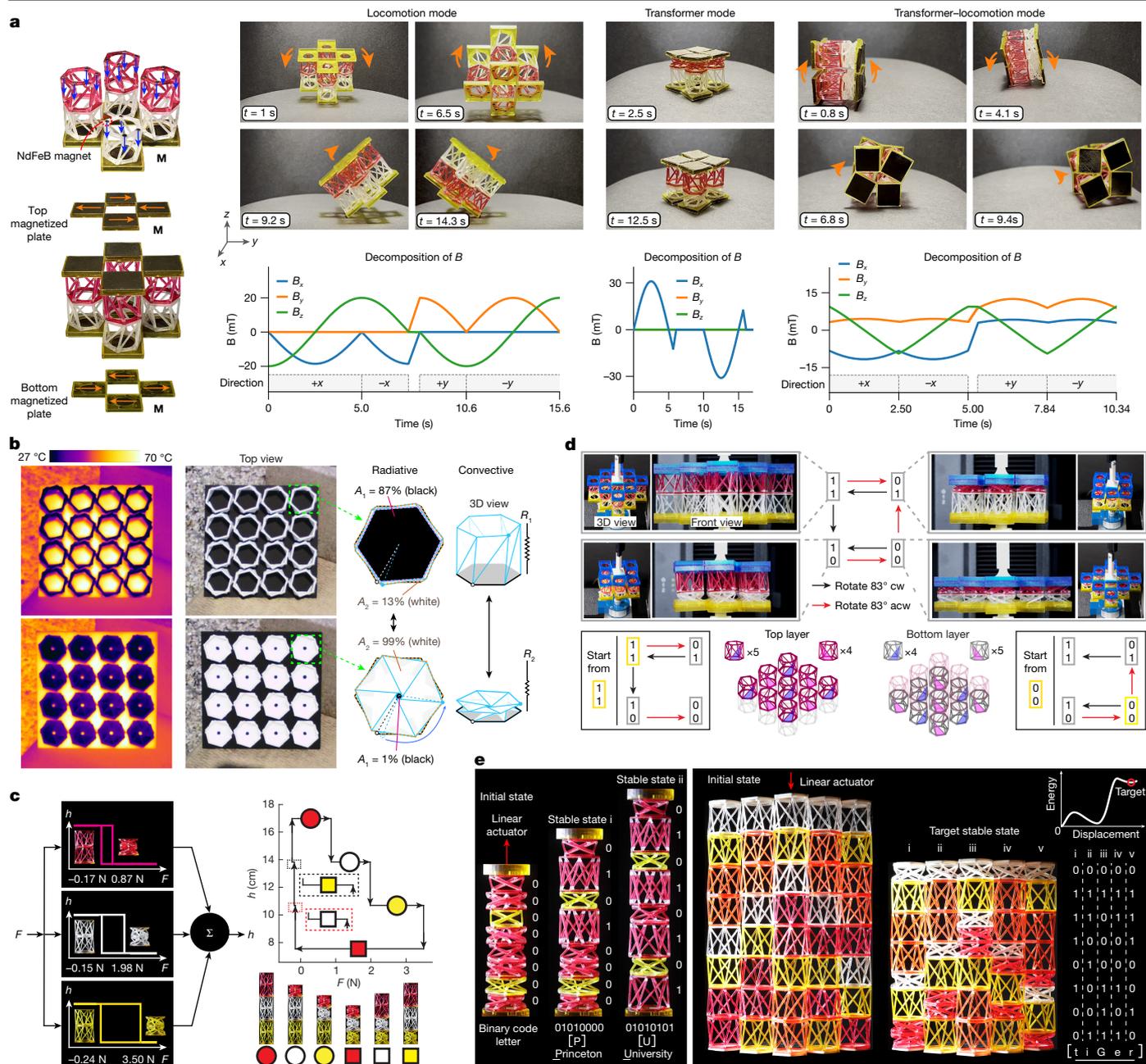
Fig. 6 | Scope of multimodal origami metamaterials. a, Magnetic robot transformer. Left, locomotion mode (robotic motion, rigid body). Centre, transformer mode (material deformation). Right, combined transformer–locomotion mode. **b**, Thermoregulation. Origami arrays with optical materials such as white radiative coolers and black solar absorbers on their facets can be used to control the amount of solar heating by controlling the fractional area of each facet type. The folded and deployed state of the origami cells can also trap various thicknesses of air, effectively allowing control over convective heat gains and losses ($R_1 > R_2$). This concept applies to thermoregulation of buildings. **c**, Preisach model with multiple connected hysterons. **d**, Non-commutativity. The dual modality of the modular chiral assembly enables its history-dependent behaviour under twist actuation. **e**, Two instances of programmable information storage/encryption. Left, an array with bistable cells. Right, large origami assembly globally actuated to reach a desired target state.

These abilities open up possibilities for untethered self-assembly as well as remote tuning of mechanical properties.

Thermoregulation

Multistable modular metamaterials hold promise for a wide range of mechano-optical functionalities. In principle, the panels of these metamaterials enable integration of a wide array of optical materials, in a variety of arrangements. Coupled with the actuation of these metamaterials, this can lead to a wide array of tunable functionalities. For instance, the integration of spectrally selective optical materials such as radiative coolers[43] and solar absorbers[44] can enable switching between modes that lose or trap thermal radiation. This can be used, for example, for tunable heating and cooling of buildings with the seasons[45]. A prototype, composed of origami units with black and white panels, with an apparent thermal tunability, is shown in Fig. 6b and Extended Data Fig. 7. By controlling the fraction of the white $A_2/(A_1 + A_2)$ and black $A_1/(A_1 + A_2)$ areas exposed to sunlight, the net albedo,

and thus the extent of solar absorption by the array, can be controlled. Thus, the origami assembly can switch between cooling (mostly white) and heating (mostly black) modes.

The mechano-optical functionalities can be further complemented by mechano-thermal tunability. By switching between folded and deployed states, multistable origami metamaterials can trap different thicknesses of air. This can control convective heat flows through or across arrays of these metamaterials, which can suppress or augment the mechano-optical or radiative functionalities as desired. For example, by suppressing convection with a thick layer of trapped air, the deployed and black prototype in Fig. 6b can prevent the convective dissipation of the absorbed solar heat, effectively increasing the thermal resistance (from R_2 to R_1) and leading to a more efficient heating. It is foreseeable that these functionalities can enable an unprecedented and multimodal thermoregulation of buildings, with potentially major impact on energy consumption (Supplementary Information section 7).

Mechanical hysterons

Hysteron is a bivalued operator with an overlapping region in which the output relies on the input history[46]. The system of multiple connected hysterons, also celebrated as the Preisach model[47], was originally used to describe magnetic hysteresis. Recently, with the development of mechanical computing[48], mechanical hysterons have been proposed to characterize memory behaviours in mechanical systems[49,50]. We demonstrate a simple but fundamental mechanical system of modular hysterons in Fig. 6c. The system is composed of three modular dipoles (Fig. 6c, left) of which red, white and yellow distinguish their critical loads switching between two heights (or called material bits[50]). For each input force F, the total height of the column is bivalued, and the true height is dependent on the loading history (see Methods, 'Mechanical hysterons', and Supplementary Information section 8).

Non-commutative state transition

The dual modality of the chiral modular metamaterial enables its history-dependent behaviour. We demonstrate its non-commutative state transition diagram in Fig. 6d for a two-layered metamaterial under twist actuation, which is validated by experiments shown in Extended Data Fig. 8. The height of each layer varies with the twist. When the series of clockwise and anticlockwise rotations are applied to the assembly at the state 11 or 00, the final state is dependent on the order of the two rotations, leading to the non-commutative state transition (see Methods, 'Non-commutative state transition', and Supplementary Video 6 for the experimental recordings of the state transition).

Information encryption

By engineering the energy barrier of the lattice units in the origami assembly, we can program the folding and deploying sequence. Considering the eight-cell array shown in Fig. 6e (left), we design the units to transition from folded state 0 to deployed state 1 sequentially. Under tensile loading, the 8-gon cells, with the lowest energy barrier, deploy first followed by the 6-gon cells. The written-in state information is not accessible before assembly and becomes evident only after axial loading. Moreover, the encrypted information is scalable by building multiple arrays into the assembly, as shown in Fig. 6e (right). We refer to Extended Data Fig. 2a for the testing setup.

Concluding remarks and discussion

We explore modular chiral metamaterials with finite multimodal deformations enabling twist, contraction and shrinkage (height change) under a single-degree-of-freedom actuation using specially designed

fixtures (Figs. 2 and 3). The multimodal deformations are associated with non-rigid origami behaviour of the Kresling pattern and with modularity of the chiral origami involving either unit cells, dipole arrangements, columnar arrays with tunable chirality or assemblies connected to kirigami-inspired planar tessellations. The supermodular system for on-the-fly material creation enables reprogrammable multistability, tunable loading capacity, scalability and multiphysics integration (for example, magnetic, thermal and optical fields). We use our findings to either unveil applications (for example, thermoregulation), theory (for example, mechanical hysterons) or to broaden the interdisciplinary scope of the work (for example, robotic metamaterials) (Fig. 6). With the integration of an untethered actuation scheme (for example, three-dimensional magnetic fields), we propose programming the assembly deformation and property on demand for micro-robotic machines.

Online content

Any methods, additional references, Nature Portfolio reporting summaries, source data, extended data, supplementary information, acknowledgements, peer review information; details of author contributions and competing interests; and statements of data and code availability are available at https://doi.org/10.1038/s41586-025-08851-0.

1. McEvoy, M. A. & Correll, N. Materials that couple sensing, actuation, computation, and communication. *Science* **347**, 1261689 (2015).
2. Mirkhalaf, M. & Rafsanjani, A. Harnessing machine mechanisms to continuously reprogram metamaterials. *Matter* **6**, 3719–3731 (2023).
3. Frenzel, T., Kadic, M. & Wegener, M. Three-dimensional mechanical metamaterials with a twist. *Science* **358**, 1072–1074 (2017).
4. Yasuda, H. et al. Origami-based impact mitigation via rarefaction solitary wave creation. *Sci. Adv.* **5**, eaau2835 (2019).
5. Gansel, J. K. et al. Gold helix photonic metamaterial as broadband circular polarizer. *Science* **325**, 1513–1515 (2009).
6. Banerjee, D., Souslov, A., Abanov, A. G. & Vitelli, V. Odd viscosity in chiral active fluids. *Nat. Commun.* **8**, 1573 (2017).
7. Fleck, N. A., Deshpande, V. S. & Ashby, M. F. Micro-architectured materials: past, present and future. *Proc. R. Soc. A Math. Phys. Eng. Sci.* **466**, 2495–2516 (2010).
8. Deshpande, V. S., Fleck, N. A. & Ashby, M. F. Effective properties of the octet-truss lattice material. *J. Mech. Phys. Solids* **49**, 1747–1769 (2001).
9. Berger, J., Wadley, H. G. N. & McMeeking, R. M. Mechanical metamaterials at the theoretical limit of isotropic elastic stiffness. *Nature* **543**, 533–537 (2017).
10. Deshpande, V. S., Ashby, M. F. & Fleck, N. A. Foam topology: bending versus stretching dominated architectures. *Acta Materialia* **49**, 1035–1040 (2001).
11. Gibson, L. J. & Ashby, M. F. *Cellular Solids: Structure and Properties* 2nd edn (Cambridge Univ. Press, 1999).
12. Jiao, P., Mueller, J., Raney, J. R., Zheng, X. & Alavi, A. H. Mechanical metamaterials and beyond. *Nat. Commun.* **14**, 6004 (2023).
13. Zheng, X. et al. Ultralight, ultrastiff mechanical metamaterials. *Science* **344**, 1373–1377 (2014).
14. Portela, C. M. et al. Supersonic impact resilience of nanoarchitected carbon. *Nat. Mater.* **20**, 1491–1497 (2021).
15. Shaikeea, A. J. D., Cui, H., O'Masta, M., Zheng, X. R. & Deshpande, V. S. The toughness of mechanical metamaterials. *Nat. Mater.* **21**, 297–304 (2022).
16. Hatch, H. W., Stillinger, F. H. & Debenedetti, P. G. Chiral symmetry breaking in a microscopic model with asymmetric autocatalysis and inhibition. *J. Chem. Phys.* **133**, 224502 (2010).
17. Feng, H. et al. Helical structures with switchable and hierarchical chirality. *Appl. Phys. Lett.* **116**, 194102 (2020).
18. Frenzel, T. et al. Large characteristic lengths in 3D chiral elastic metamaterials. *Commun. Mater.* **2**, 4 (2021).
19. Choi, G. P. T., Dudte, L. H. & Mahadevan, L. Programming shape using kirigami tessellations. *Nat. Mater.* **18**, 999–1004 (2019).
20. Misseroni, D. et al. Origami engineering. *Nat. Rev. Methods Primers* **4**, 40 (2024).
21. Blees, M. K. et al. Graphene kirigami. *Nature* **524**, 204–207 (2015).
22. Schroeder, T. B. H. et al. An electric-eel-inspired soft power source from stacked hydrogels. *Nature* **552**, 214–218 (2017).
23. Bertoldi, K., Vitelli, V., Christensen, J. & van Hecke, M. Flexible mechanical metamaterials. *Nat. Rev. Mater.* **2**, 17066 (2017).
24. Cui, J. et al. Nanomagnetic encoding of shape-morphing micromachines. *Nature* **575**, 164–168 (2019).
25. Overvelde, J. T. B., Weaver, J. C., Hoberman, C. & Bertoldi, K. Rational design of reconfigurable prismatic architected materials. *Nature* **541**, 347–352 (2017).
26. Hu, Z. et al. Engineering zero modes in transformable mechanical metamaterials. *Nat. Commun.* **14**, 1266 (2023).
27. Melancon, D., Gorissen, B., García-Mora, C. J., Hoberman, C. & Bertoldi, K. Multistable inflatable origami structures at the metre scale. *Nature* **592**, 545–550 (2021).
28. Overvelde, J. T. B. et al. A three-dimensional actuated origami-inspired transformable metamaterial with multiple degrees of freedom. *Nat. Commun.* **7**, 10929 (2016).

29. Li, Y. et al. Adaptive hierarchical origami-based metastructures. *Nat. Commun.* **15**, 6247 (2024).
30. Kim, Y., Yuk, H., Zhao, R., Chester, S. A. & Zhao, X. Printing ferromagnetic domains for untethered fast-transforming soft materials. *Nature* **558**, 274–279 (2018).
31. Kim, Y. & Zhao, X. Magnetic soft materials and robots. *Chem. Rev.* **122**, 5317–5364 (2022).
32. Xia, X., Spadaccini, C. M. & Greer, J. R. Responsive materials architected in space and time. *Nat. Rev. Mater.* **7**, 683–701 (2022).
33. Jenett, B. et al. Discretely assembled mechanical metamaterials. *Sci. Adv.* **6**, eabc9943 (2020).
34. Chen, T., Pauly, M. & Reis, P. M. A reprogrammable mechanical metamaterial with stable memory. *Nature* **589**, 386–390 (2021).
35. Zhang, Y., Velay-Lizancos, M., Restrepo, D., Mankame, N. D. & Zavattieri, P. D. Architected material analogs for shape memory alloys. *Matter* **4**, 1990–2012 (2021).
36. Liu, K., Pratapa, P. P., Misseroni, D., Tachi, T. & Paulino, G. H. Triclinic metamaterials by tristable origami with reprogrammable frustration. *Adv. Mater.* **34**, 2107998 (2022).
37. Schenk, M. & Guest, S. D. Geometry of miura-folded metamaterials. *Proc. Natl Acad. Sci. USA* **110**, 3276–3281 (2013).
38. Liu, K. & Paulino, G. H. Nonlinear mechanics of non-rigid origami: an efficient computational approach. *Proc. R. Soc. A Math. Phys. Eng. Sci.* **473**, 20170348 (2017).
39. Rafsanjani, A., Bertoldi, K. & Studart, A. R. Programming soft robots with flexible mechanical metamaterials. *Sci. Robot.* **4**, eaav7874 (2019).
40. Cui, H. et al. Design and printing of proprioceptive three-dimensional architected robotic metamaterials. *Science* **376**, 1287–1293 (2022).
41. Yoder, Z., Rumley, E. H., Schmidt, I., Rothemund, P. & Keplinger, C. Hexagonal electrohydraulic modules for rapidly reconfigurable high-speed robots. *Sci. Robot.* **9**, eadl3546 (2024).
42. Baines, R., Fish, F., Bongard, J. & Kramer-Bottiglio, R. Robots that evolve on demand. *Nat. Rev. Mater.* **9**, 822–835 (2024).
43. Yin, X., Yang, R., Tan, G. & Fan, S. Terrestrial radiative cooling: using the cold universe as a renewable and sustainable energy source. *Science* **370**, 786–791 (2020).
44. Mandal, J. et al. Scalable, "dip-and-dry" fabrication of a wide-angle plasmonic selective absorber for high-efficiency solar-thermal energy conversion. *Adv. Mater.* **29**, 1702156 (2017).
45. Mandal, J. et al. Porous polymers with switchable optical transmittance for optical and thermal regulation. *Joule* **3**, 3088–3099 (2019).
46. Visintin, A. *Differential Models of Hysteresis* (Springer, 2013).
47. Preisach, F. Über die magnetische nachwirkung. *Z. Phys.* **94**, 277–302 (1935).
48. Yasuda, H. et al. Mechanical computing. *Nature* **598**, 39–48 (2021).
49. Mungan, M. Putting memories on paper. *Proc. Natl Acad. Sci. USA* **119**, e2208743119 (2022).
50. Liu, J. et al. Controlled pathways and sequential information processing in serially coupled mechanical hysterons. *Proc. Natl Acad. Sci. USA* **121**, e2308414121 (2024).

Methods

Basic modules and properties

Geometry. The chiral cells are derived from the Kresling origami[51]. This shell-based origami has multiple crease skeletons, for example, see two representatives highlighted as white dashed lines in Extended Data Fig. 1a (left). We translate those origami creases into rod members[52,53] to create the rod-based lattice unit shown in Extended Data Fig. 1a (right). Each modular cell, for example, 6-gon cell, has two stable configurations, that is, one in the deployed state and the other in the folded state (Extended Data Fig. 1b). During the transition between the two stable states, the height of the unit changes along with the twist of the top polygon. The two representative twist angles, φ_1 and φ_0, are highlighted as two local minimum points in the strain energy envelope (Extended Data Fig. 1c). The energy is calculated using equations (4)–(7), which will be introduced later. Based on geometrical compatibility between the two stable configurations, we derive the analytical expressions for φ_0 and φ_1 as (Supplementary Information section 1)

$$\varphi_1 = \arccos\left(\frac{h_1^2 - h_0^2}{4r^2}\sec\frac{\pi}{n}\right) - \frac{\pi}{n}, \quad \varphi_0 = \pi - \frac{2\pi}{n} - \varphi_1. \tag{2}$$

Here, n is the number of polygon edges, r is the polygon radius and h_1 and h_0 are the heights of the unit in the folded state and the deployed state, respectively. From a design perspective, equation (2) indicates that the geometry is determined by four independent parameters, that is, h_1, h_0, n and r. Those geometry parameters need to satisfy the following design constraint[54] to avoid the locking stage where valley rods collide in the folded state:

$$|h_1^2 - h_0^2| \le 4r^2\cos^2\frac{\pi}{n}. \tag{3}$$

For the 6-gon Kresling cell used in this work, we define deployed height $h_1 = 28.3$ mm, folded height $h_0 = 12.6$ mm and polygon radius $r = 16.8$ mm.

Chirality. Chirality is an independent parameter that does not rely on the height or twist angle. In other words, for the given height and twist angle, the Kresling cell can always have two configurations corresponding to two reversed chirality +1 and −1 (Supplementary Fig. 17). The chirality is essentially determined by the way of connecting the top and bottom basis of the unit cells. For example, in Fig. 1f (left), each valley rod (the longest edge of the blue or red triangle) connects the top and bottom basis in the reverse manner. For the cell featuring anticlockwise rotation, the valley rod connects one node of the bottom base and the next node of the top base in the anticlockwise direction. By contrast, for the cell featuring clockwise rotation, the valley rod connects one node of the bottom base and the next node of the top base in the clockwise direction. The connection does not rely on any geometric parameter such as height or twist angle.

Deformation coupling. The Kresling cells have coupled translational and rotational deformation. The linear displacement and the twisting of the Kresling cells are locally coupled because the applied torsion (with twisting) can trigger linear displacement and the applied force (with linear displacement) can trigger twisting deformation. The modular arrays and assemblies inherit the coupled translational and rotational deformation from the Kresling cells.

Dipole. A dipole (for example, in Figs. 5b and 6c) is composed of two cells with opposite chirality. When a dipole is compressed, its middle layer can rotate freely. If we consider half of the dipole, this phenomenon resembles the linear displacement with free-rotation boundary condition for compressing a unit cell. We have used this free-rotation feature in constructing the mechanical hysterons (Fig. 6c and Supplementary Fig. 14a). As shown in Supplementary Fig. 14a, the free rotation triggers the bistable deformation profile and causes the correspondence between a single value of force and multiple values of height. This multivalued mapping is the key to constructing a hysteron. If the free rotation is suppressed, that is, the middle layer cannot rotate freely, the multivalued mapping disappears (Supplementary Fig. 14b). In this case, it is impossible to achieve the mechanical hysteron with the Kresling dipole.

Kinematic compatibility. The twist of the modular unit is designed to be kinematically compatible with the twist of the tessellations on the top and bottom of the assembly. The maximum rotation angle of the rotating-square tessellation is 90°. Thus, the change of rotation angle $\Delta\varphi$ for the cell needs to be less than or equal to 90°. For the present 6-gon cell, $\Delta\varphi = |\varphi_0 - \varphi_1| = 83° < 90°$.

Generalization. The unit cell geometry can be generalized from shell-based origami to rod-based lattice unit (Extended Data Fig. 1) to incorporate various regular polygons as the top and bottom faces. For example, Fig. 1e shows sample geometry of 4-gon, 6-gon and 8-gon units considering the rod-based lattice model (see a verification example for the 4-gon geometry using an inverse design scheme in Supplementary Information section 9 and Supplementary Fig. 12). For unit cells with a given geometry, we can obtain desired cell properties with proper chirality assignments and material selections. Accounting for both the chirality and the energy barrier aspects at the unit cell level, we can program the global deformation of the metamaterial. We refer to a case study in Supplementary Information section 10 and Supplementary Fig. 13 that elaborates on preferred design features in the Kresling cells leading to desired multimodal deformation.

Experiments

Materials and manufacturing. The origami-inspired unit cells (magenta, blue, white and yellow), hinged tessellations (yellow and blue) and assembly plates (white) are fabricated using a multimaterial PolyJet 3D printer (Stratasys J55 prime). Unit cells are made of two components, that is, rods and soft joints, which are 3D-printed using materials with different elastic modulus (Supplementary Fig. 15). The materials used to print the rods are VeroMagentaV, VeroCyanV, VeroUltraClear and VeroYellowV, which have a similar elastic modulus $E \approx 2.2$ GPa (https://www.stratasys.com/en/materials/materials-catalog/polyjet-materials/verovivid/). The soft joints are made of digital materials created during printing by mixing VeroUltraClear and ElasticoClear. More specifically, the materials used to print the joints of units in magenta or blue, white and yellow are FLXA9950 (Shore-A 50), FLXA9970 (Shore-A 70) and FLXA9985 (Shore-A 85), respectively. Using the formula Modulus = exp(Shore-A × 0.0235 − 0.6403), the elastic modulus of the soft joints is 1.7 MPa, 2.7 MPa and 3.9 MPa, respectively (ref. 55).

Mechanical tests. We have designed multiple experimental setups to validate the mechanical properties of the origami arrays and assemblies under axial and rotational loading. The tests (Figs. 2, 3 and 6d, Extended Data Figs. 5 and 8 and Supplementary Figs. 4–7 and 16) are conducted by an Instron 68SC-5 equipped with a biaxial load cell (±445 N, ±5.65 N m). The tests (Figs. 5 and 6e and Supplementary Figs. 9–11) are performed using an Instron 5944 equipped with a load cell (±2 kN).

We conduct rotational tests at 2° s⁻¹ loading rate. The rotational actuation with free translation enables a twist of the origami assembly while allowing it to undergo axial folding and deploying without any constraint. The central square connector (attached to the top rotating-square tessellation) translates freely and is connected to a linear railing system through the use of a slider (Extended Data Fig. 2b).

Article

In this test, we measure the edge change ratio and height change ratio manually using snapshots from the video recordings of the experiments.

We conduct linear displacement tests at 20 mm min^{-1} loading rate. The linear displacement actuation with free rotation (Extended Data Fig. 2c) enables axial deformation on the origami assembly while allowing the top tessellation to rotate without any constraint. This is achieved through the ball bearings (connected to the top plate) and ball transfers (connecting the tessellations to the plates). The ball transfers are used to markedly reduce friction between the tessellations and plates (Extended Data Fig. 2c, middle and right). Here, we film the tests using a camera (Sony ILME-FX6V, Lens: FE 24-105mm F4 G OSS) and measure the height change ratio and twist angle by tracking the markers through a Python script using the OpenCV library. The edge change ratio is calculated by the formula $\cos(\varphi/2) - 1$, where φ is the measured twist angle (Supplementary Information section 2).

We use the standard axial setup to perform compression tests at 20 mm min^{-1} loading rate (Extended Data Fig. 2a). Moreover, we calculate the energy in this test (denoted by U_{exp}) using the displacement D_{exp} and load F_{exp} measured from the Instron machine, according to the following expression $U_{exp} = \sum_{i=1}^{n} (D_{exp,i+1} - D_{exp,i-1}) F_{exp,i}/2$, where n denotes the number of experimental data points.

Actuation decoupling. Although the Kresling cells, arrays and assemblies have coupled translational and rotational deformation, the actuation is decoupled. Specifically, the actuation can be decoupled into twist with free translation and linear displacement with free rotation provided the proper experimental setup is designed (Figs. 2 and 3, respectively). The aim of decoupling the twisting and translation in actuation is to avoid the undesired reaction force or torque induced from the locally coupled deformation: under the twist actuation with free translation, we have only the active torque and avoid the reaction force; under the linear displacement actuation with free rotation, we have only the active force and avoid the reaction torque. In other words, the decoupled actuation leads to simplified loading conditions, which is the key to capturing the large deformation of the multimodal origami metamaterial.

Magnetic tests. A custom-made 3D Helmholtz-coil system comprising 12 individual copper windings is used to generate the required magnetic field for the wireless actuation of the robotic metamaterial (Extended Data Fig. 6 and Supplementary Information section 6). We design and construct a 25-kW power electronic drive optimized for this particular coil system to independently control the current of each winding pair. To achieve precise control of the currents and eliminate any sensitivity to environmental and operating conditions, we implement a closed loop current-control scheme on a microcontroller control card. The magnetic field calibration is performed using a vector Gaussmeter instrument (Gaussmeter Model VGM AlphaLab). The soft square magnetic plates installed on the top and bottom tessellations are made of 80% by weight compound of 25 micron Nd-Pr-Fe-B alloy powder (Magnequench MQFP 15-7) and silicone rubber (Ecoflex 00-30). An impulse magnetizer (ASC Scientific MODEL IM-10-30) is used to ensure proper magnetization of the plates. Further details about the magnetic elements and the electromagnetic actuation setup are provided in the Extended Data Fig. 6 and Supplementary Information section 6.

The fundamental actuation principle behind all three modes of motion, that is, locomotion, transformer and transformer–locomotion, is the exertion of electromagnetic torques. When a dipole of magnetic moment **m** is subjected to an externally imposed flux density **b**, a torque $\tau = \mathbf{m} \times \mathbf{b}$ is exerted. In this regard, the coupling of the translational and rotational motions is the important property enabling the magnetic actuation of the metamaterial. Leveraging the rotational–translational coupling, deformation is achieved through the application of torques on the individual tessellation squares without the presence of translational forces. This deformation mechanism allows for magnetic actuation and provides extended control flexibility through the appropriate placement and orientation of the square magnetic plates. The transformer–locomotion mode constitutes an example highlighting the opportunities emerging from the rotational–translational coupling: on the one hand, the size of the robot is reduced allowing the access of confined spaces; on the other hand, a net in-plane magnetization emerges because of the twisting of the tessellation squares allowing the locomotion of the contracted robot around its out-of-plane axis.

Thermoregulation tests. A multistable modular assembly is fabricated from white origami paper (TANT) against a black foamboard (Fome-Cor Pro), such that the origami cells themselves cover 70% of the total area of the assembly. The origami cells are then deployed to expose more black area—of the 70% covered by cells, 88% is black and 12% is white. The array is then positioned to directly face the sun for 5 min to heat up the assembly. A thermal image is taken with a FLIR T865 thermal camera, with the imaging angle close to the angle of incidence of sunlight. The origami cells are then quickly folded to expose more white area, so that of the 70% covered by cells, 1% is black and 99% is white, and then exposed to sunlight again and subjected to thermographing, in an identical manner to the deployed state. Furthermore, the single-layer assembly can be extended to a dipole assembly for enhancing thermal resistance (Supplementary Fig. 18).

Simulation: bar and hinge model

Bar and hinge model is a simple but computationally efficient approach (compared with finite element analysis) that can capture the global deformation of non-rigid origami structures[37,38]. Inspired by this approach, we propose a surrogate model for quick and insightful investigations of the nonlinear deformations of our multimodal metamaterial at different levels: unit cell, column and assembly with rotating-square tessellations.

Unit cell. We assume that the strain energy of the modular prototypes is stored in the soft joints. Stretching of the soft joints along the mountain and valley rods (of lengths b and c; Supplementary Fig. 1) causes the effective length change of these rods (that is, the total length change of a rod and the soft joints at both ends of the rod). We denote this stretching energy by U_m. Ideally, the rod lengths are determined by the height h and twist angle φ of the modular cell, and therefore U_m is a function of h and φ. However, the deformation of the real prototypes is complicated because of the bending and shearing of the soft joints and the contact of rods. These effects may also produce energy, resisting the modular cell from overall twisting and compression. Based on this consideration, we introduce two additional energy terms U_h and U_t, which are assumed to depend on the overall height change and twisting, respectively. Then, the total strain energy of the modular cell (denoted by U_{cell}) can be written as

$$U_{cell}(h, \varphi) = U_m(h, \varphi) + U_h(h) + U_t(\varphi). \tag{4}$$

The three energy terms correspond to different spring components in the surrogate model (Extended Data Fig. 3a,b). With $U_{cell}(h, \varphi)$, we can formulate optimization problems to simulate deformations of the modular cells under twist with free translation or compression with free rotation (Extended Data Fig. 3c,d and Supplementary Information section 5). We denote the mountain and valley rod stiffness by k_b and k_c, respectively. Then, U_m can be written as

$$U_m(h, \varphi) = \frac{nk_b}{2}[\tilde{b}(h, \varphi) - b]^2 + \frac{nk_c}{2}[\tilde{c}(h, \varphi) - c]^2. \tag{5}$$

The deformed rod lengths $\tilde{b}(h,\varphi)$ and $\tilde{c}(h,\varphi)$ are given in Supplementary Information section 1. We denote the overall compression stiffness by k_h. Then, U_h is defined as

$$U_h(h) = \begin{cases} \dfrac{k_h}{2}(h-h_1)^2, & h \geq h_0, \\ c_s k_h \left(\dfrac{1}{h} - \dfrac{h^2}{h_0^3} + \dfrac{3h}{h_0^2} - \dfrac{3}{h_0} \right) + \dfrac{k_h}{2}(h-h_1)^2, & 0 < h < h_0, \end{cases} \quad (6)$$

It is worth noting that we have added the (c_s/h) term to U_h for $h < h_0$. The coefficient c_s is assigned a large number $(1 \times 10^6 \text{ mm}^3$ in this work), so that the cell becomes extremely stiff to compression after the second stable state. This setting simulates the fact that the cell cannot be completely compressed to zero height because of the contact of the rods of finite thickness. The other terms (h^0, h^1, h^2) for $h < h_0$ are used to make U_h continuous at h_0 up to the second-order derivative. We denote the overall twisting stiffness by k_t. Then, U_t is defined as

$$U_t(\varphi) = \frac{k_t}{2}(\varphi - \varphi_1)^2. \quad (7)$$

We determine the values of various stiffness defined above based on the experimental compression loading curves for the cells of different materials (Supplementary Fig. 16). Specifically, we solve a multiobjective goal attainment problem to seek the match of the peak forces between experiments and the simulation (Supplementary Information section 5). In Extended Data Fig. 3a, the red, white and yellow cells are assigned the mountain rod stiffness $k_b = 0.5442$, 1.2828 and 2.2080 N mm^{-1}; the overall stiffness $k_h = 0.0100$, 0.0300 and 0.0300 N mm; and $k_t = 0.0106$, 0.0258, 0.0448 N mm rad^{-1} for the red, white and yellow cells, respectively. In Fig. 1g, the red and white cells are assigned $k_b = 0.5442$ and 1.2828 N mm^{-1}, respectively, and both cells are assigned $k_h = 0$ and $k_t = 0$. In Extended Data Fig. 1c,d, the cell is assigned $k_b = 0.5442$ N mm^{-1}, $k_h = 0$ and $k_t = 0$. For all 6-gon unit cells, the valley rod stiffness is calculated as $k_c = k_b b/c$. The geometry is set according to the real prototypes. Specifically, we assign $a = 16.8$ mm, $b = 28.8$ mm, $c = 35.4$ mm, $h_1 = 28.3$ mm, $h_0 = 12.6$ mm, $\varphi_1 = 18.7°$ and $\varphi_0 = 101.3°$ (see Supplementary Fig. 1 for the illustration of these notations).

Column. The strain energy of a column (denoted by U_{column}) can be obtained by simply adding up the energy of each modular cell:

$$U_{\text{column}}(h,\varphi) = \sum_k U_{\text{cell},k}[h_k(h,\varphi), \varphi_k(h,\varphi)]. \quad (8)$$

With U_{column}, we can simulate the deformations of the column under the twist with free translation or compression with free-rotation loading (Supplementary Information section 5). To perform the twist simulation in Extended Data Fig. 4a,b, we apply the following constraint to the total twist angle of the column: $\sum_{k=1}^3 (\varphi_k c_k) = \bar{\varphi}$. The parameter c_k prescribes the chirality (bivalued +1 or −1) of the kth unit cell. The total twist angle $\bar{\varphi}$ constrains the summation of the twist angles for all layers $c_k \varphi_k$ ($k = 1, 2, 3$). We change $\bar{\varphi}$ in the following sequence: first anticlockwise twisting from 0 to $-(\varphi_0 - \varphi_1) = -83°$ in 100 steps, then clockwise twisting from −83° to 83° in 200 steps, resulting in a cumulative twist angle 249°. To perform the compression simulation in Extended Data Fig. 4c,d, we apply the following constraint to the total height of the column: $\sum_{k=1}^3 h_k = \bar{h}$. The total height $\bar{h}$ constrains the summation of the heights for all layers h_k ($k = 1, 2, 3$), and is uniformly decreased from $3h_1 = 84.9$ mm to $3h_0 = 37.8$ mm, which is controlled by the displacement loading from 0 to $3(h_1 - h_0) = 47.1$ mm in 300 steps.

Assembly. For the assembly with rotating-square tessellations, the rotational stiffness of the tessellations (denoted by k_{RS}) also contributes to the total strain energy (denoted by U_{assembly}). Therefore, U_{assembly} can be written as

$$U_{\text{assembly}}(h,\varphi) = \sum_{k'} U_{\text{column},k'}(h,\varphi) + \frac{k_{\text{RS}}}{2}\varphi^2. \quad (9)$$

With U_{assembly}, we can simulate the deformation of the assembly under the twist with free translation or compression with free-rotation loading (Supplementary Information section 5). We assign $k_{\text{RS}} = 90$ N mm rad^{-1} for the twist loading (Fig. 4a–e) or 288 N mm rad^{-1} for the compression loading confined by two plates (Fig. 4f–j). With these stiffness assignments, the final strain energy matches between simulation and experiment for either the twisting (Fig. 4d) or the compression loading (Fig. 4i). The higher value of k_{RS} in the compression loading with two plates essentially reflects the stiffness increase of the metamaterial caused by the constraint from the plates. For the compression loading with no plate (Supplementary Fig. 8a–c), the stiffness is consistent with the twist loading (which involves no plate, too), that is, $k_{\text{RS}} = 90$ N mm rad^{-1}. In this case, the simultaneous folding of red and white cells (which happens in the compression loading with two plates) does not exist in both simulation (Supplementary Fig. 8a–c) and experiment (Supplementary Fig. 5).

Folding sequence control. In reality, in addition to geometry, chirality and material composition, the folding sequence of cells depends on the random defects from the fabrication process. This is the reason why random folding happens during the experiment. For example, in Fig. 2b, at step (3), some of the unit cells in the middle layer are folded, whereas some in the top layer are folded. However, in simulation (Fig. 4b), all unit cells in the top layer are folded at step (3). As we cannot predict the randomness a priori, we avoid the randomness by disturbing the stiffness of layers of the same material. Thus, for different layers of the columns or assemblies, if their materials (that is, the colours) are the same, we disturb the rod stiffness by a small value (for example, $\epsilon = 0.001$ N mm^{-1}) to control the order of folding. Specifically, for the column with three red cells (Extended Data Fig. 4b,d, first row), k_b of the bottom and the middle layers is increased by 2ϵ and ϵ, respectively; for the column with two red cells (Extended Data Figs. 4b,d, second row, and 5a, top row), k_b of the top layer is increased by ϵ; for the column with two white cells (Extended Data Figs. 4b,d, third row, and 5a, bottom row), k_b of the bottom layer is increased by ϵ; for the assemblies in Fig. 4 and Supplementary Fig. 8d–f, k_b of the middle layer is increased by ϵ; for the assembly in Supplementary Fig. 8a–c, k_b of the top layer is increased by ϵ.

Mechanical hysterons

The bistability nature of the modular origami cells makes them promising candidates for mechanical hysterons (Fig. 6c). For each dipole, in the overlapping region between two critical forces, the output (bivalued height) relies on the input history. That is, the height h of the dipole is high if the force F is on the left of the overlapping region and is low if the force F is on the right of the overlapping region. In other words, the dipoles 'remember' the deformation they have experienced. The mechanical Preisach model is built by summing up the output of the three hysterons reacting to the same input force, describing a mechanical hysteresis loop passing through six (but not all) possible configurations of a column of the three dipoles that are serially connected (Fig. 6c, right). The detailed formulation for the Preisach model is provided in Supplementary Information section 8.

Non-commutative state transition

The twist with free translation actuation enables the non-commutative state transition of the modular chiral assembly (Fig. 6d). The twist loading is applied to the centre column of the assembly. In the centre column, the white cell has the chirality such that it can be compressed only

Article

under clockwise twisting, and the red cell has reversed chirality such that it can be compressed only under anticlockwise twisting. For the other columns, the chirality is consistent with that in the centre such that they are compressed or deployed synchronously. A two-bit number is used to indicate the four possible states of the assembly: 11, 00, 01 and 10, with the first bit corresponding to the red layer and the second bit corresponding to the white layer. For each bit, the digit 1 indicates that the layer is deployed and the digit 0 indicates that the layer is compressed. When the two layers are both deployed (11) or both compressed (00), the deformation of the metamaterial is dictated by the chirality of the cells, regardless of their different stiffness. Specifically, starting from the fully deployed state 11, clockwise twisting compresses the white layer and anticlockwise twisting compresses the red layer. Starting from the fully compressed state 00, clockwise twisting expands the red layer and anticlockwise twisting expands the white layer. In short, from state 00 or 11, the metamaterial can go to either state 10 or 01 under the proper direction of twisting. Then, the non-commutativity arises at the intermediate state 01 or 10, which allows only the transition to one other state. We first consider state 01, which represents the compressed red layer and the deployed white layer. Because of the specific chirality of the red and white cells, clockwise twisting can expand the red layer or compress the white layer, whereas anticlockwise twisting cannot change the state 01. The actual result depends on the stiffness of the red and white cells. In our demonstration, the white cells are stiffer than the red cells, so a larger torque is required to change the state of the white layer compared with the red layer. As a result, state 01 can only go to state 11 under clockwise twisting. For the same reason, state 10 can go only to state 00 under anticlockwise twisting. Extended Data Fig. 8 shows the experimental loading curves and the values of torques that are required to trigger the state transition of the red and white layers. Altogether, when a series of clockwise and anticlockwise rotations is applied to the metamaterial at the state 11 or 00, the final state is dependent on the order of the two rotations, leading to the non-commutative state transition. We refer to Supplementary Video 6 for the experimental recordings of the state transitions.

Data availability

The experimental data supporting the findings of this study are openly available at Zenodo[56] (https://doi.org/10.5281/zenodo.14676200). Source data are provided with this paper.

Code availability

The simulation codes supporting the findings of this study are openly available at Zenodo[56] (https://doi.org/10.5281/zenodo.14676200).

51. Kresling, B. Natural twist buckling in shells: from the Hawkmoth's bellows to the deployable Kresling-pattern and cylindrical Miura-ori (2008). In *Proc. 6th International Conference on Computation of Shell and Spatial Structures IASS-IACM: "Spanning Nano to Mega"* (eds Abel, J.F. & Cooke, J. R.) 18–21 (Cornell Univ. Press, 2008).
52. Yasuda, H., Tachi, T., Lee, M. & Yang, J. Origami-based tunable truss structures for non-volatile mechanical memory operation. *Nat. Commun.* **8**, 962 (2017).
53. Zhai, Z., Wang, Y. & Jiang, H. Origami-inspired, on-demand deployable and collapsible mechanical metamaterials with tunable stiffness. *Proc. Natl Acad. Sci. USA* **115**, 2032–2037 (2018).
54. Lang, R. J. *Twists, Tilings, and Tessellations: Mathematical Methods for Geometric Origami* (CRC Press, 2017).
55. Qi, H., Joyce, K. & Boyce, M. Durometer hardness and the stress-strain behavior of elastomeric materials. *Rubber Chem. Technol.* **76**, 419–435 (2003).
56. Paulino, G. H. et al. Super-modular chiral origami metamaterials. *Zenodo* https://doi.org/10.5281/zenodo.14676200 (2025).
57. Zang, S., Misseroni, D., Zhao, T. & Paulino, G. H. Kresling origami mechanics explained: experiments and theory. *J. Mech. Phys. Solids* **188**, 105630 (2024).

Extended Data Fig. 1 | Modular lattice cell geometry. a, From standard shell-based origami to the rod-based lattice unit. Visual comparison between a paper-folded Kresling origami (left) and a 3D-printed lattice prototype (right). The diameter of the rods is 1.5 mm (scale bar, 5 mm). **b**, Schematic of a 6-gon unit in the deployed state (left) and in the folded state (middle). The top view (right) of the unit highlights two twist angles, φ_1 and φ_0, which define the position of the top polygon in the two stable states. h_1, deployed unit height; h_0, folded unit height; u, displacement; c, valley rod length; b, mountain rod length; r, polygon radius. **c**, The strain energy of the unit versus twist angle obtained with the bar-and-hinge method. **d**, The height of the unit versus twist angle.
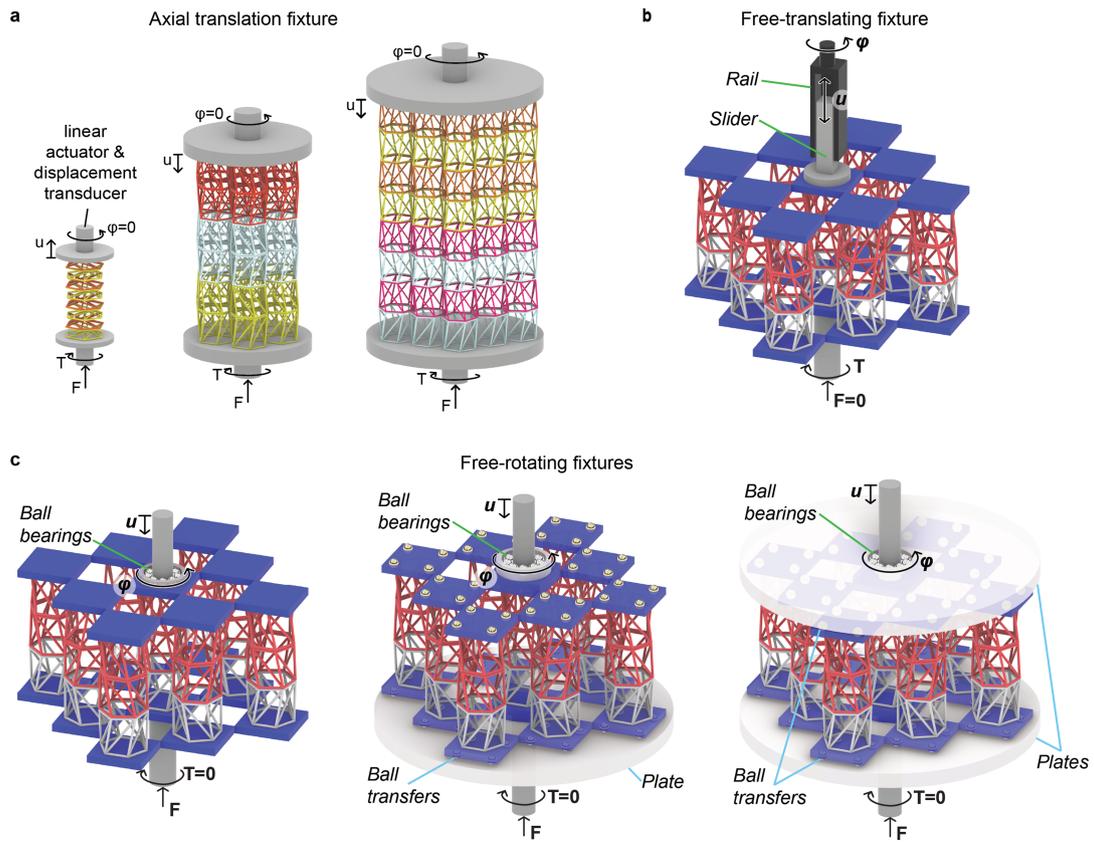
Extended Data Fig. 2 | Schematics of mechanical test setups: boundary conditions and loading conditions. a, Axial translation fixture for standard tests with displacement control. Left and right: for results in left and right of Fig. 6e, respectively. Middle: for Fig. 5. **b**, Dedicated fixture for rotational test with free translation[57]. This fixture is used for obtaining results in Figs. 2, 6d, Extended Data Fig. 8, and Supplementary Fig. S4. **c**, Alternative fixtures for linear displacement with free rotation. Left: Supplementary Fig. S5. Middle: Supplementary Fig. S6. Right: Fig. 3 and Supplementary Fig. S7.
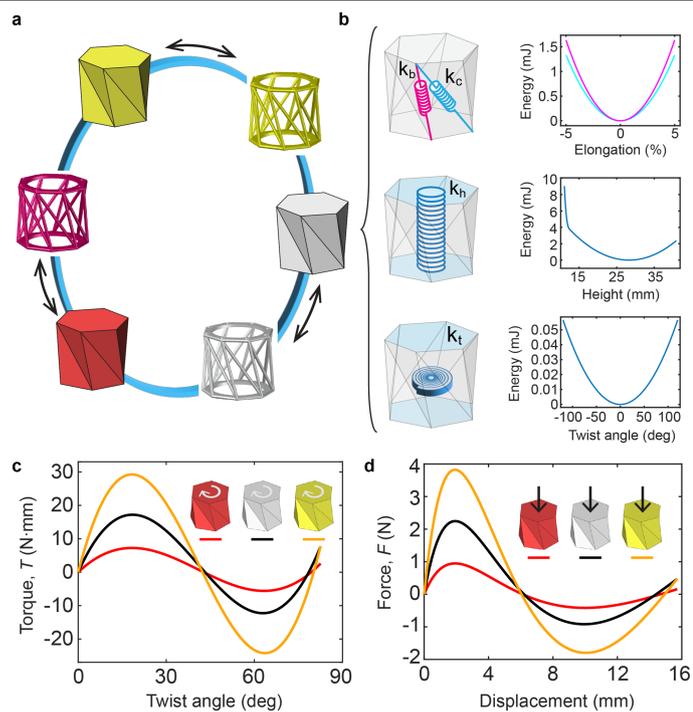
Extended Data Fig. 3 | Surrogate model simulation for multimodal deformations of the chiral modular cells. a, The modular cells (frames) and the origami models (shells). **b**, Mechanical springs in the surrogate model. **c**, Torque-twist-angle curves from the twisting simulation of three cells of the same geometry but different material properties. **d**, Force-displacement curves from the compression simulation of three cells of the same geometry but different material properties.
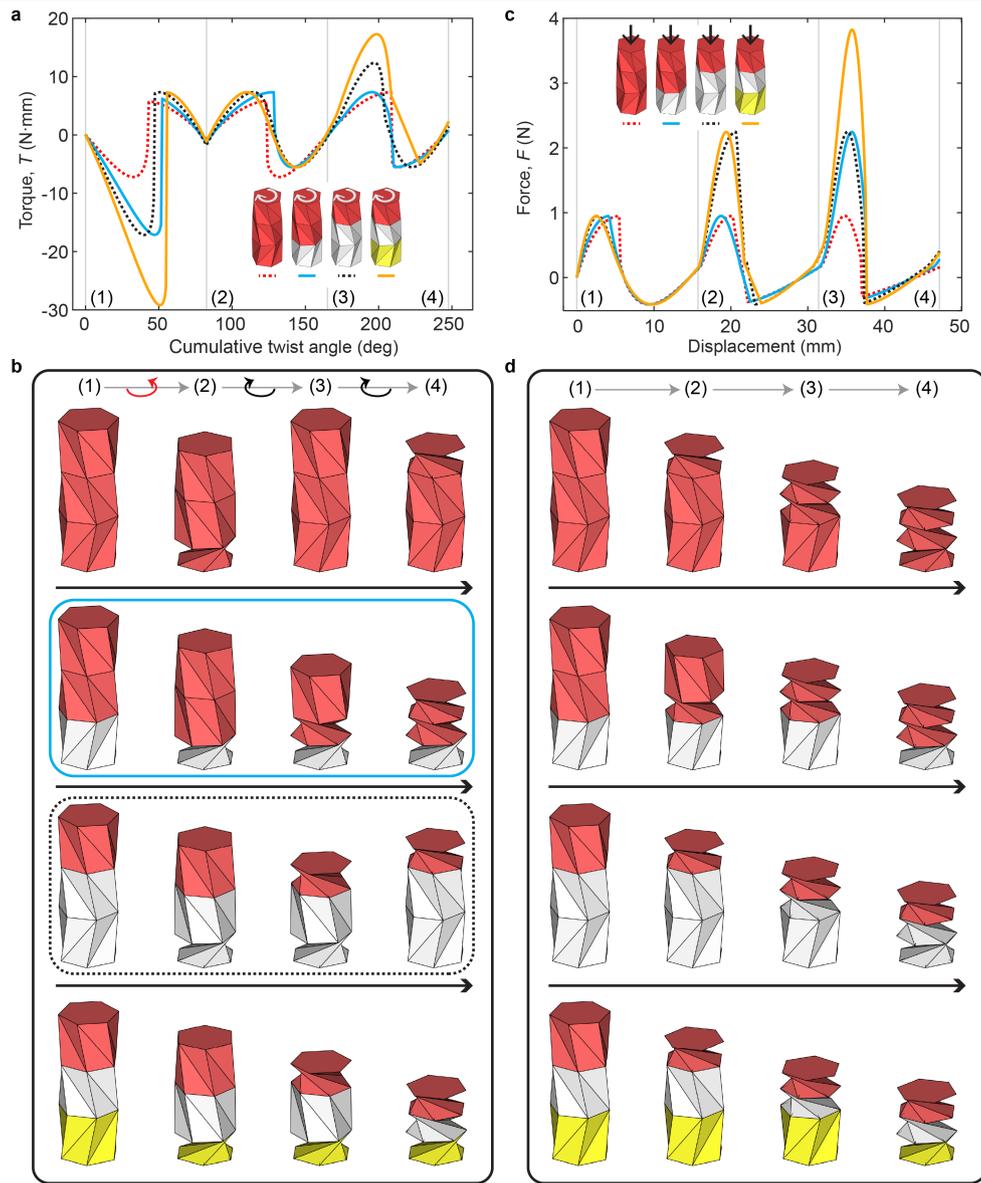
Extended Data Fig. 4 | Surrogate model simulation for multimodal deformations of the chiral modular columns with different constituent cells. **a**, Torque versus cumulative twist angle from the twisting simulation of the columns. **b**, Deformation snapshots of the twisted columns. The two boxes indicate the configurations with corresponding experimental results (Extended Data Fig. 5). **c**, Force versus displacement from the compression simulation of the columns. **d**, Deformation snapshots of the compressed columns.
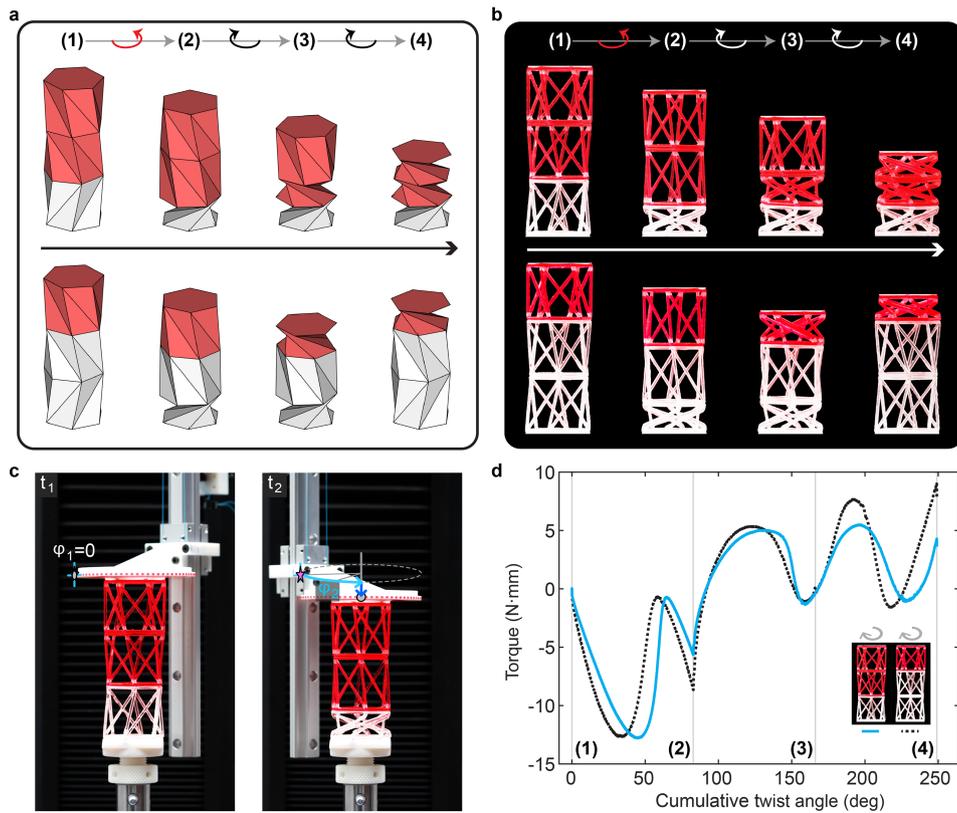
Extended Data Fig. 5 | Twisting experiments of two columns that differ by their chiral modular arrangement and material composition. a, Surrogate model simulations. **b**, Experimental results. **c**, Snapshots illustrating the twisting experiment with free translation. **d**, Experimental results of torque versus cumulative twist angle.
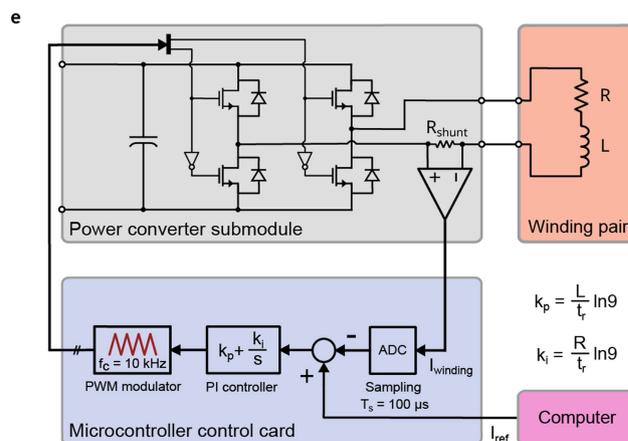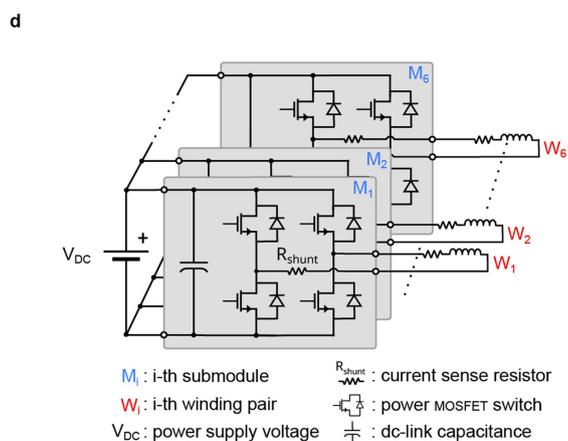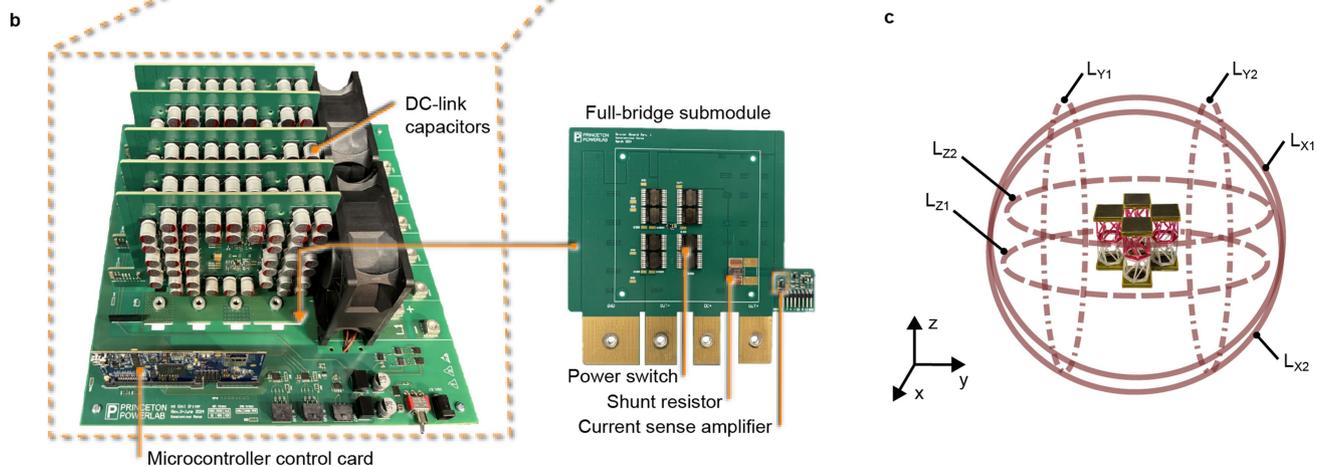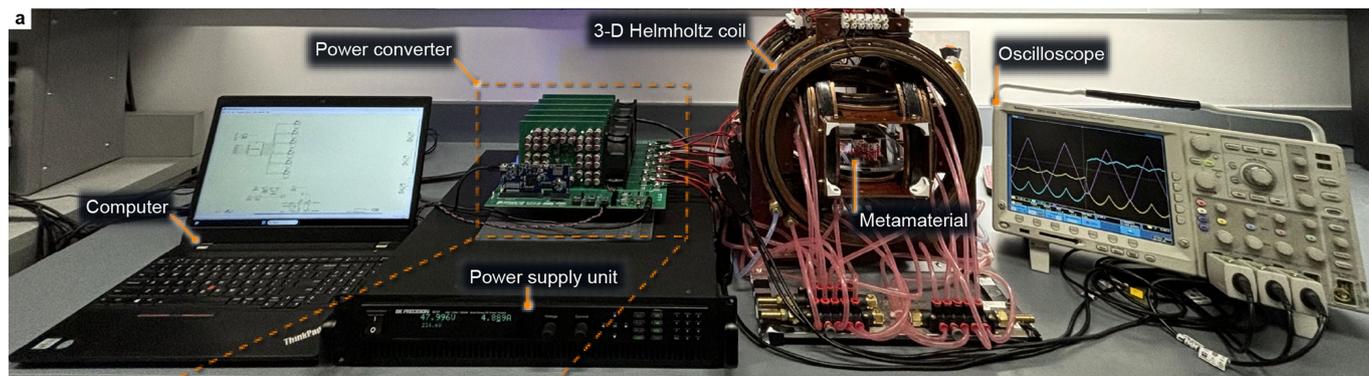
Extended Data Fig. 6 | Electrical system for the precise control of the magnetically actuated robotic metamaterial. a, Experimental setup consisting of a dc power source, a scalable power converter, and a set of copper coils. **b**, Modular power converter prototype comprising six individual power electronic building blocks. **c**, 3-D Helmholtz coil structure made of six circular-winding pairs; each pair consists of two windings connected in series. **d**, Scalable power-converter topology consisting of six full-bridge submodules to precisely control the current of each winding pair. **e**, System block diagram showing the closed loop current-control scheme; the winding currents are sensed locally in each submodule using shunt resistors. A proportional-integral controller is implemented on a microcontroller card resulting in an equivalent first order reference-to-winding current system. Each coil is modeled by an inductance value L and a resistance R representing the resistivity of the copper wire. The controller gains are selected as $k_p = L/t_r \ln 9$ and $k_i = R/t_r \ln 9$ to accomplish a 10% to 90% current rise time of $t_r = 1.5$ ms. A pulse width modulator (PWM) employing a 10 kHz triangular carrier wave is used to generate the signals controlling the states of the individual power switches.

a Deployed state

a=25 mm
h₁=42 mm

$a = 25\ \text{mm}$
$h_1 = 42\ \text{mm}$

b Folded state

200 mm
φ=102 deg
h₀=9 mm

$\varphi = 102\ \text{deg}$
$h_0 = 9\ \text{mm}$

c Calculation of deployed state

Input

a ◇25
h1/a   1.68
h0/a   ●0.36
φ
102.036141

XY Plane   Origin   Plane

h*x   X Y Z   Vector   Length

Plane / Radius / 6-gon / Corner — Bottom polygon — Polygon / Length

Base / Angle / Plane — Top polygon — Geometry / Transform

x π*(120-x)/360

Calculation of deployed state — Height / Bottom / Top — Panels / Creases / Curve 1 / Curve 2

Inside Line — Vertices / Closed
Outside Line — Vertices / Closed

Inside area — Area / C
Whole area — Area / C

x/y*100

Output
Panel model
Truss model
Inside area
Outside area
Black area
86.740547

Perspective view — Top view — Outside (white) & inside (black) areas from the top view

— creases
— panels
— black area
— white area

d Calculation of folded state

Input

a ◇25
h1/a   1.68
h0/a   ●0.36
φ
102.036141

XY Plane   Origin   Plane

h*x   X Y Z   Vector   Length

Plane / Radius / 6-gon / Corner — Bottom polygon — Polygon / Length

Base / Angle / Plane — Top polygon — Geometry / Transform

x π*(120+x)/360

Calculation of folded state — Height / Bottom / Top — Panels / Creases / Curve 1 / Curve 2

Inside Line — Vertices / Closed
Outside Line — Vertices / Closed

Inside area — Area / C
Whole area — Area / C

x/y*100

Output
Panel model
Truss model
Inside area
Outside area
Black area
0.78796

Perspective view — Top view — Outside (white) & inside (black) areas from the top view

— creases
— panels
— black area
— white area

Extended Data Fig. 7 | The optically augmented multistable origami assembly. a, Digital image of the prototype in the deployed state. **b**, Prototype in the folded state. **c**, Interactive algorithm for parametric modelling with calculation of the origami cell in the deployed state. **d**, Interactive algorithm for parametric modelling with calculation of the origami cell in the folded state.
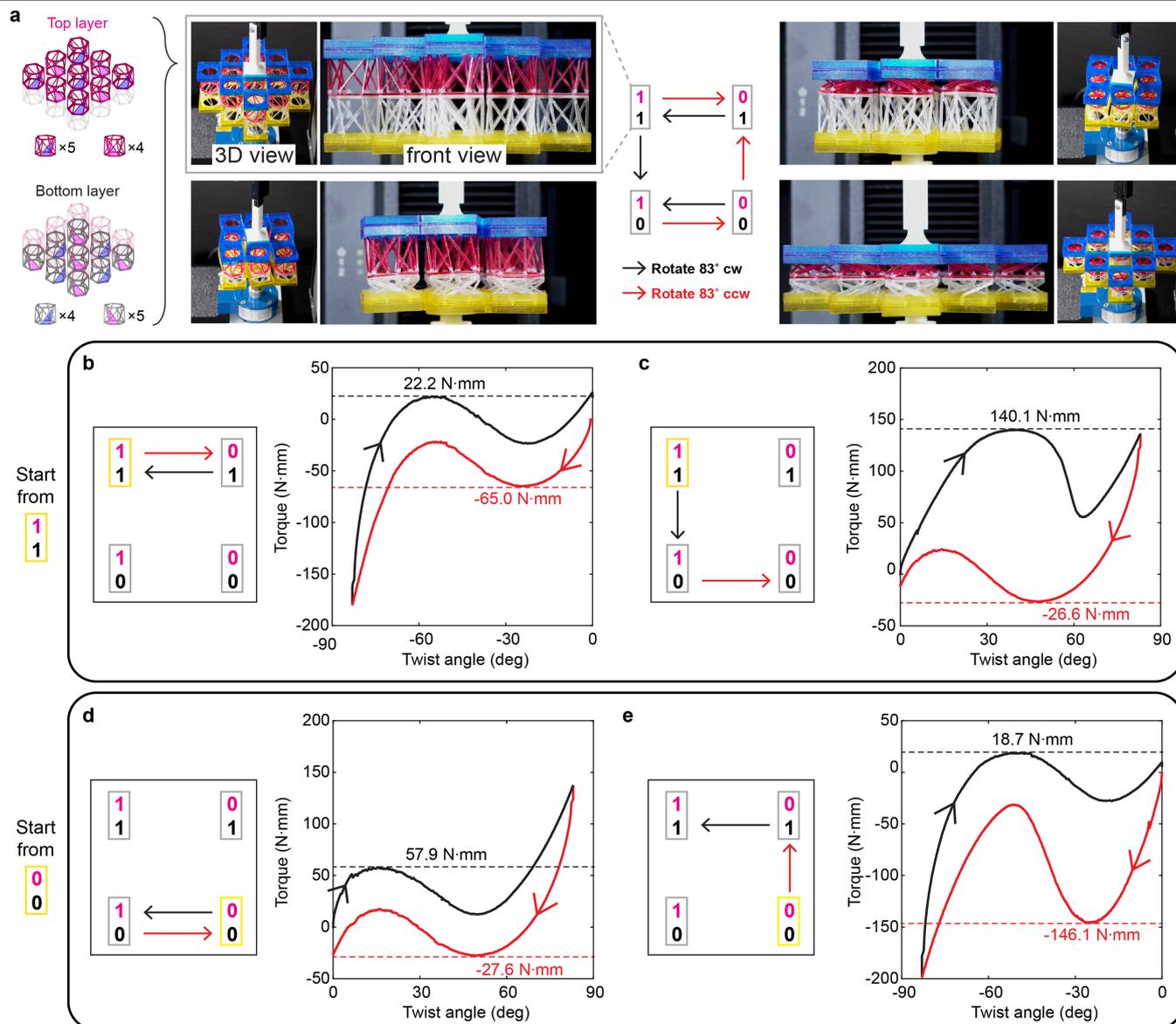
Extended Data Fig. 8 | Non-commutative state transition of the two-layer chiral metamaterial. a, The possible states of the metamaterial. A two-bit number is used to indicate the global states, with each bit representing an entire layer. For each bit, the digit 1 indicates that the layer is deployed, and the digit 0 indicates that the layer is folded. **b**–**e**, Experimental loading curves for state transitions (b) starting from 11 with a anticlockwise rotation followed by a clockwise rotation, (c) starting from 11 with a clockwise rotation followed by a anticlockwise rotation, (d) starting from 00 with a clockwise rotation followed by a anticlockwise rotation, (e) starting from 00 with a anticlockwise rotation followed by a clockwise rotation. The peak torques that trigger the state transitions are indicated in the plots.